



# Band-type resonance: non-discrete energetically optimal resonant states

Arion Pons · Tsevi Beatus

Received: 21 April 2022 / Accepted: 2 September 2022 / Published online: 14 October 2022  
© The Author(s), under exclusive licence to Springer Nature B.V. 2022

**Abstract** Structural resonance involves the absorption of inertial loads by a tuned structural elasticity: a process playing a key role in a wide range of biological and technological systems, including many biological and bio-inspired locomotion systems. Conventional linear and nonlinear resonant states typically exist at specific discrete frequencies and specific symmetric waveforms. This discreteness can be an obstacle to resonant control modulation: deviating from these states, by modulating waveform asymmetry or drive frequency, generally leads to losses in system efficiency. Here, we demonstrate a new strategy for achieving these modulations at no loss of energetic efficiency. Leveraging fundamental advances in nonlinear dynamics, we characterise a new form of

structural resonance: band-type resonance, describing a continuous band of energetically optimal resonant states existing around conventional discrete resonant states. These states are a counterexample to the common supposition that deviation from a linear (or nonlinear) resonant frequency necessarily involves a loss of efficiency. We demonstrate how band-type resonant states can be generated via a spectral shaping approach: with small modifications to the system kinematic and load waveforms, we construct sets of frequency- and asymmetry-modulated resonant states that show equal energetic optimality to their conventional discrete analogues. The existence of these non-discrete resonant states in a huge range of oscillators—linear and nonlinear, in many different physical contexts—is a new dynamical systems phenomenon. It has implications not only for biological and bio-inspired locomotion systems but for a constellation of forced oscillator systems across physics, engineering, and biology.

---

A. Pons (✉) · T. Beatus (✉)  
The Silberman Institute of Life Sciences, Faculty of  
Science, Hebrew University of Jerusalem,  
Giv'at Ram, Jerusalem, Israel  
e-mail: arion.pons@mail.huji.ac.il

T. Beatus  
e-mail: tsevi.beatus@mail.huji.ac.il

A. Pons · T. Beatus  
The Benin School of Computer Science and Engineering,  
Hebrew University of Jerusalem, Giv'at Ram, Jerusalem,  
Israel

A. Pons · T. Beatus  
The Grass Bioengineering Center, Faculty of Science,  
Hebrew University of Jerusalem, Giv'at Ram, Jerusalem,  
Israel

**Keywords** Structural resonance · Energy  
resonance · Global resonance · Energetic optimality ·  
Nonlinear mechanics · Biomimetic propulsion

## 1 Introduction

Resonance is a phenomenon which is both complex and ubiquitous. In a classical mechanics context, structural resonance represents both a harmonic coupling effect between structural inertia and structural elasticity; and a fundamental characteristic of linear oscillators and linear operators [1–3]. This same characteristic generalises to many forms of nonlinear oscillator and extends to a wide range of other physical contexts: fluid mechanics [4–6], optomechanics [7–9], electrical circuits [10–13], plasma waves [14, 15], and further [16–18]. Nonlinear resonant phenomena come in many forms and typically generalise certain optimality properties of linear resonance: optimality in amplitude response [12, 16, 19, 20], optimality in energy transfer [20–26], etc. Even focusing on a structural or mechanical context, linear and nonlinear resonance are of core importance to many technological and biological systems: microelectromechanical (MEMS) oscillators [27–31]; atomic force microscopes [32–35]; piezoelectric shunt absorbers [36–38]; elastic metamaterials [26, 39, 40]; the locomotive structures of a huge range of airborne [41–47], aquatic [48–53], and legged organisms [54]; and a correspondingly wide range of bio-inspired locomotive technologies [55–67].

Resonant states are typically discrete, in some sense: linear second-order oscillators have certain discrete eigenstates, and discrete transfer function peaks [1–3]. Linear resonant states exist at certain discrete frequencies and simple-harmonic input/output waveforms. Nonlinear resonant states—of which there are several different forms—can show more complex behaviour: they may exist at complex multiharmonic excitation and response states, and may vary their frequency and waveform with excitation/response amplitude, as in the Duffing oscillator [11, 16, 68]. Nevertheless, these nonlinear resonant states are still discrete in the sense that, at a given amplitude, certain discrete resonant frequencies exist. The discreteness of linear and nonlinear resonant states can be an obstacle to system control. Consider, for instance, classical-mechanical resonant behaviour within biological and bio-inspired locomotive systems. If the nominal state of locomotion is resonant, then it should be impossible to modulate the frequency of the locomotive output response, or modulate the level of asymmetry in the output waveform, without

the penalty of leaving the state of resonance—namely, without compromising on efficiency and perfect inertial load absorption [44, 45]. These forms of locomotive resonant response modulation can also be seen as a unique, and less well-studied, form of active or semi-active vibration control. Contrary to classical active [69–73] and semi-active [74–76] approaches, the control objective is not to minimise the vibrational response of a system, but to maximise it—and, in the ideal case, to maintain the efficiency of a discrete resonant state over a continuous band of modulated states. Making this ideal case a reality may appear impossible, given the intrinsic discreteness of classical resonance—for this reason, biological and bio-inspired locomotive resonance is often considered to place restrictions, for example, on modulation of the locomotive response frequency and asymmetry [20, 44, 46].

This apparent restrictiveness is all the more interesting because it is defied in practice. Several species of insect which are thought to utilise resonance to generate a propulsive wingbeat response do engage in significant wingbeat frequency modulation—in both a controlled [44, 77–80] and seemingly stochastic [81] manner. Asymmetry modulation is also observed: in these species, orientation control is regularly achieved via modulation of the asymmetry of the wingbeat response [82–84]. If an insect flight motor is modelled as a linear oscillator with fixed structural properties [20, 85], then frequency modulation and asymmetry modulation appear inconsistent with maintaining a resonant state: they represent changes in the equilibrium point and natural frequency of the oscillator, respectively. Accounting for known nonlinearities in insect flight motors (e.g. quadratic aerodynamic damping) does not itself significantly alter this apparent inconsistency [20]. Proposed explanations have instead focused on the operation of sets of auxiliary flight muscles, which could potentially allow real-time control of thoracic structural resonant properties [44, 46, 86–89], making the flight motor into a time-varying linear or nonlinear system, and thereby potentially allowing wingbeat frequency and asymmetry modulation while maintaining a resonant state. Alternatively, this modulation has been explained in terms of the trade-off between deviating from resonance, and achieving other goals, such as performing a harsh manoeuvre [44], or engaging in courtship [90]. This trade-off could involve switching between

different system resonant frequencies (displacement, velocity resonance, etc.); as well as the particular behaviour of energy resonance, i.e. global resonance [20–25], which shows a particularly low cost associated with frequency deviation [20]. In addition, nonlinear (e.g. Duffing-type) effects could lead to certain forms of amplitude-coupled resonant frequency modulation [20, 42]. Aspects of these proposed explanations are still unclear—for instance, given that wingbeat amplitude modulation (which maintains linear resonance) is available for apparently the same purpose as frequency modulation (which disrupts linear resonance), it is not clear why the latter should ever have evolved [44, 46, 77].

In this work, we shed new light on the practical and theoretical limits of resonant state modulation. *Firstly*, we show how resonant states can be non-discrete: in both linear and nonlinear systems, an energy resonant state [20–25] are available not only at discrete eigenstates, but within a band of frequencies and symmetry-broken waveforms around these states. These non-discrete states—the *band-type resonant states*—generalise the energetic properties of a linear eigenstate to non-harmonic input/output waveforms: states ensure that actuator power consumption is minimised. In classical-mechanical systems with linear inertia, they ensure that the system inertia makes no contribution to the overall actuator power consumption—i.e. that this power consumption is determined solely by the power dissipation of dissipative elements in the system. The existence of this space of non-discrete resonant states has not previously been identified. *Secondly*, we demonstrate how band-type resonant states can be generated via an advanced excitation strategy: small modifications to the system drive waveforms, for example, in the form of spectral shaping, can be utilised to generate targeted resonant modulations in frequency or output symmetry. We demonstrate both analytical and numerical methods for carrying out this spectral shaping process. These methods lead to novel strategies for energetically optimal resonant state modulation, and thereby, new control principles for linear and nonlinear systems. These control principles can be seen as forms of model-based active vibration control that maximise, rather than minimise, the energy transfer of an actuator to a system. We illustrate, with examples, how these control principles are applicable to a range of linear and nonlinear oscillators—and how, more

specifically, they enable forms of energetically optimal locomotive frequency and asymmetry modulation in biolocomotion systems such as flapping-wing aircraft. *Finally*, we illustrate how these new control principles provide new explanations for counterintuitive biolocomotive behaviour. In the specific context of insect flight motor resonance, band-type resonance quantitatively explains resonant frequency variation effects observed in several insect species. In this way, the phenomenon of band-type resonance is shown to have significance across theoretical and applied dynamics: as a counterpoint to the assumed discreteness of resonant states; as a control principle for forced oscillators; and as a practical tool for understanding and designing biolocomotion systems.

## 2 Dynamics of PEA and SEA systems

### 2.1 System configurations

Consider a general single-degree-of-freedom (1DOF) system, with general nonlinear time-invariant dynamics. The system is driven by an actuator, which provides some force,  $F(t)$ , and thereby generates a system displacement,  $x(t)$ . In general, we are interested in cases in which  $F(t)$  and  $x(t)$  are oscillatory. The equation of motion of this system is given by:

$$D(x, \dot{x}, \ddot{x}, \dots) = F(t), \quad (1)$$

where  $D(\cdot)$  expresses the system's time-invariant dynamics. Equation 1 can be used to model a huge range of different physical processes: not only mechanical systems, such as insect flight motors [20, 42–47] and MEMS devices [27–30]; but also, electrical [10–13], and other [16, 18] processes.

Consider then introducing a conservative force into Eq. 1: a force,  $F_s(x)$ , dependent solely on displacement, or, in structural terms, an elastic element. Introducing this elastic element can lead to two distinct system configurations: parallel-elastic actuation (PEA), in which the actuator and elastic element are connected in parallel; and series-elastic actuation (SEA), in which the actuator and elastic element are connected in series (Fig. 1A, B). The equations of motion of these two configurations may be expressed:

$$\begin{aligned} \text{PEA: } D(x, \dot{x}, \ddot{x}, \dots) + F_s(x) &= F(t), \\ \text{SEA: } D(x, \dot{x}, \ddot{x}, \dots) &= F_s(u - x) = F(t), \end{aligned} \quad (2)$$

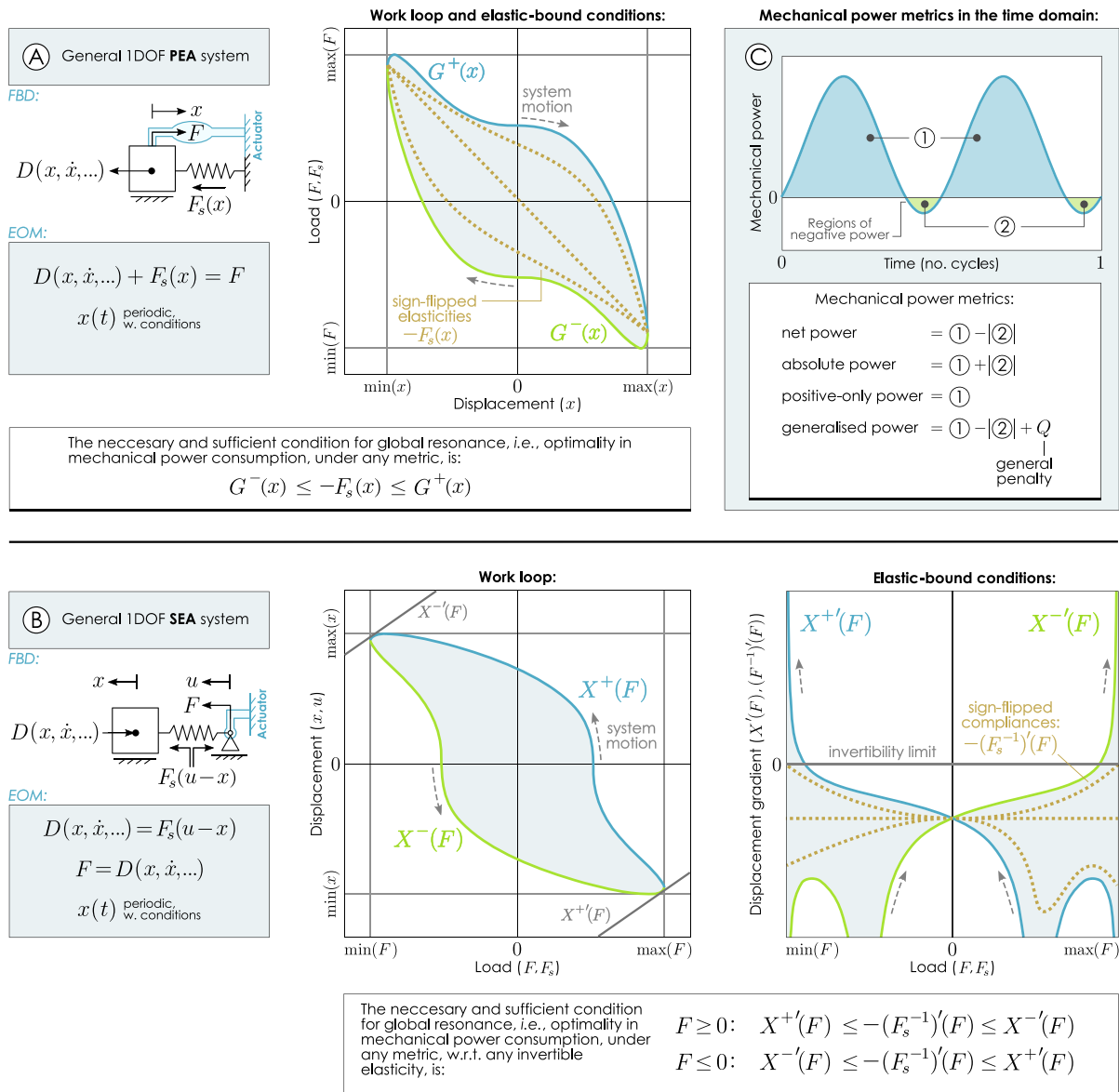


**Fig. 1** Schematic of general PEA and SEA systems, and their respective elastic-bound conditions. **A** A general nonlinear 1DOF PEA system, with the elastic-bound conditions for energy resonance illustrated on the system work-loop (Eq. 3). **B** A general nonlinear 1DOF SEA system, with the system work-loop illustrated in the rotated work-loop space (Eq. 4), and the

elastic-bound conditions for energy resonance illustrated in the relevant derivative space (Eq. 6). **C** Explanation of the four metrics of mechanical power consumption—net, absolute, positive-only and generalised, as per Eq. 5—with a representative time-domain power requirement

where  $F_s(x)$  is the conservative force, which may show a nonlinear dependence on  $x$ ; and  $u(t)$  is the displacement of the system actuator, or actuation point, which in the SEA configuration may be distinct from  $x(t)$ . We note that the system dynamics,  $D(\cdot)$ , may already express some conservative force, which

in the PEA case may function identically to  $F_s(x)$ . The choice between PEA and SEA configurations is a design question found frequently in robotics [91, 92], and a distinguishing factor between many forms of physical system [20, 27].

To analyse the oscillatory behaviour of these general nonlinear systems, we use work-loop analysis

techniques [25]. First, consider that  $x(t)$ , the system motion, is given (prescribed, or desired) as some periodic (i.e. steady-state) time-domain profile. Then, in the PEA system, it is possible to compute  $F(t)$ , which is also periodic, and visualise it against  $x(t)$ : a visualisation as a steady-state work loop, in the plane  $F$ – $x$ . In a general system undergoing general motion, this work loop may be complex—indeed, it may not be a closed loop. We restrict ourselves to a certain subset of system behaviour: we require that this work loop in  $F$ – $x$ : (a.i) is a closed simple curve (i.e. no self-intersection); (a.ii) is no more than bivalued at any  $x$ ; and (a.iii) represents net power dissipation (i.e. the progression of time must represent clockwise travel around the closed loop). A corollary of condition (a.ii) is the simpler condition that the given periodic  $x(t)$  must be composed of two monotonic curves over its period: it must vary monotonically from  $\max(x)$  to  $\min(x)$ ; and monotonically from  $\min(x)$  back to  $\max(x)$ . Under conditions (a.i)–(a.iii), the steady-state work loop ( $F$  vs.  $x$ ) permits a representation as two single-valued curves:  $F^+(x)$  and  $F^-(x)$  (Fig. 1A, with examples in “Appendix A.1”). A proof of this representation can be found in [25]; intuitively, if the loop is no more than bivalued for any  $x$ , then two curves can represent the loop over  $x$ . Correspondingly, we can devise the same representation the inelastic load,  $G(t) = D(x, \dot{x}, \ddot{x}, \dots)$ , via Eq. 2. If  $F^+(x)$  and  $F^-(x)$  exist, as per conditions (a.i)–(a.iii), then  $G^+(x)$  and  $G^-(x)$  also exist. Substituting  $F^\pm(x)$  for  $F(t)$  and  $G^\pm(x)$  for  $D(x, \dot{x}, \ddot{x}, \dots)$  in Eq. 2 yields the work-loop form of the PEA system [25]:

$$\text{PEA: } F^\pm(x) = G^\pm(x) + F_s(x). \quad (3)$$

The work-loop formulation of an SEA system is analogous. Again, consider that  $x(t)$  is given as some periodic time-domain profile. Then, we may directly compute  $F(t)$ , which is also periodic, and visualise the system work loop in the (rotated)  $x$ – $F$  plane. We again require, as analysis conditions, that this steady-state work loop: (b.i) is a closed simple curve; (b.ii) is no more than bivalued at any  $F$ ; and (b.iii) represents net power dissipation (i.e. the progression of time must represent counterclockwise travel around the closed loop). Again, a corollary of condition (b.ii) is the simpler condition that the computed periodic  $F(t)$  must be composed of two monotonic curves over its period: it must vary monotonically from  $\max(F)$  to

$\min(F)$ ; and monotonically from  $\min(F)$  back to  $\max(F)$ . Note that this split monotonicity condition on  $F(t)$  can be satisfied even when  $x(t)$  does not satisfy this same condition. The SEA steady-state work loop ( $x$  vs.  $F$ ) then also permits a representation as two single-valued curves:  $X^+(F)$  and  $X^-(F)$  (Fig. 1B, and “Appendix A.1”). We can do the same to the curves of  $u$  versus  $F$ , and represent them as  $U^+(F)$  and  $U^-(F)$ . If we assume that the elastic profile  $F_s(\cdot)$  is invertible—inverse  $F_s^{-1}(\cdot)$ —then we can rearrange Eq. 2 into an additive relationship between  $u(t)$  and  $x(t)$ ; and then substitute  $U^\pm(F)$  and  $X^\pm(F)$ , respectively, to obtain the work-loop form of the SEA system [25]:

$$\begin{aligned} \text{SEA: } u(t) &= x(t) + F_s^{-1}(F(t)) \\ U^\pm(F) &= X^\pm(F) + F_s^{-1}(F). \end{aligned} \quad (4)$$

In the SEA system, the requirement that  $F_s(\cdot)$  be invertible is a condition on our analysis. This invertibility condition still permits us to analyse range of physically relevant nonlinear elastic behaviour (e.g. strain-hardening, strain-softening, freeplay behaviour) in SEA systems, but does preclude a few other physically relevant behaviours (e.g. bistable elastic behaviour). Further generalisation of the work-loop analysis methodology in [25] is required in order to permit the analysis of non-invertible  $F_s(\cdot)$ . Finally, the analogy between Eqs. 3–4 may be noted: both represent the sum of an inelastic work loop ( $G^\pm(x)$ ,  $X^\pm(F)$ ) and an elastic profile ( $F_s(x)$ ,  $F_s^{-1}(F)$ ), yielding an elastic work loop ( $F^\pm(x)$ ,  $U^\pm(F)$ ). Fundamentally, this SEA work-loop formulation is a direct analogue of the work-loop formulation in PEA systems, except in a rotated plane ( $x$  against  $F$ , rather than  $F$  against  $x$ ). The reason for this rotation is related to the opposite relationships between power consumption and elasticity in PEA and SEA systems. In both PEA and SEA systems, the power consumption of the actuator is  $P(t) = F(t)\dot{u}(t)$ , for actuator force  $F(t)$  and velocity  $\dot{u}(t)$ . In the PEA system, if the output,  $x(t)$ , is prescribed, then the actuator velocity  $\dot{u}(t) = \dot{x}(t)$  is independent of elasticity; whereas  $F(t)$  is dependent (Eq. 2). On the other hand, in the SEA system, if output,  $x(t)$ , is prescribed, then the load  $F(t)$  is independent of elasticity; whereas  $\dot{u}(t) \neq \dot{x}(t)$  is now dependent (Eq. 2). Thus, when studying the effect of elasticity on system work loops,  $x$  is the natural independent variable for PEA systems; and  $F$  is the natural independent variable for SEA systems.



In practical terms, the analysis conditions outlined above—(a.i)–(a.iii) for the PEA system, and (a.i)–(a.iii) for the SEA system—describe an interesting set of nonlinear dynamic behaviour. They encompass a limited set of behaviour (certain periodic outputs) across a wide range of systems (any nonlinear time-invariant 1DOF PEA and SEA system). Many biologically and technologically relevant structures can be described by these nonlinear 1DOF systems—for instance, many forms of biological and bio-inspired locomotion system, such as bipedal legs [54, 60, 62, 64, 65] and flapping wings [20, 42, 45, 63, 93]. Within these locomotion systems; the particular periodic outputs encompassed by the conditions (i)–(iii) are highly relevant to locomotive behaviour: periodic flapping; or walking kinematics, which are typically composed of two monotonic curves (cf. insect wingbeat [77, 94] and bipedal walking [54, 64, 65] kinematics); and often represent dissipative work loops (cf. [94, 95]). As such, this work-loop analysis is an ideal tool to study energetically optimal forms of resonant locomotion—a particular application case that we will consider in more detail. Note that our approach to these systems, and to work-loop analysis in general, can be described as an inverse-problem approach: the desired output kinematics are defined, and then the required input loads are computed. Work-loop analyses, both in biomechanics [96, 97] and as a theoretical tool [25], typically use such an inverse-problem approach. It allows a wide range of complex nonlinear systems to be analysed—the system dynamics  $D(x, \dot{x}, \ddot{x}, \dots)$  need not be solved in a forward-problem sense, but only computed for specified  $x(t)$ —and also, in many practical biological locomotive systems, the output response is directly observable (e.g. flapping-wing kinematics), whereas the input loading required to generate this response is not, and must be estimated by modelling, cf. [95, 98]. From an analysis perspective, an inverse-problem approach will allow us to directly identify band-type resonant states in a very wide range of nonlinear systems; though this will come at the cost of reduced insight into forward-problem effects (e.g. sensitivity to system and input disturbances) in these resonant states.

## 2.2 Energy resonance

The work-loop forms of Eqs. 3–4 allow a characterisation of the state of energy resonance in these general PEA and SEA systems. Energy resonance, or global resonance, is a form of linear and nonlinear resonance that is closely related to mechanical power consumption [20–25]. In intuitive terms, the state of energy resonance is a state in which power flows only from the actuator to the system, and never in reverse: in a linear PEA 1DOF system, the energy resonant frequency coincides with the system natural frequency, but in other systems, these frequencies may differ [20]. In more formal terms, the time-domain actuator mechanical power consumption,  $P(t)$ , is given by  $P = F\dot{x}$  in the PEA system, and  $P = F\dot{u}$  in the SEA system.  $P(t)$ , may contain regions of both positive ( $P > 0$ ) and negative ( $P < 0$ ) power: positive power represents power flow from the actuator to the system; and negative power, the reverse. Energy resonant states are those in which  $P(t) \geq 0, \forall t$ . We note that condition of non-negative power flow,  $P(t) \geq 0, \forall t$  is not something that can be specified a priori in a system undergoing forced oscillation. For instance, specifying a unidirectional actuator force input ( $F \geq 0$ ) never guarantees an energy resonant state ( $F\dot{x} \geq 0$ ), because the system response ( $\dot{x}$ ) may oscillate. Locating and characterising energy resonant states is, in general, a non-trivial exercise.

In this vein, recent results [25] have shown that energy resonance can be seen not only in terms of power flow, but in terms of power minimisation: energy resonant states form the solution to a particular power minimisation problem. Consider a nonlinear 1DOF PEA or SEA system, undergoing prescribed periodic motion,  $x(t)$ , of period  $T$ . If the system elasticity, or conservative force,  $F_s(\cdot)$ , could be chosen, then what choice(s) of elasticity would minimise the overall mechanical power consumption associated with this prescribed motion? This question is formulated as an inverse problem: finding  $F_s(\cdot)$  for a given  $x(t)$  that minimises power consumption. The overall power consumption of a system can be expressed as an integral of  $P(t)$ , but the details of this integral are actuator-specific, depending on how the actuator behaves under negative power [94, 99, 100]. In general, four classes of metrics,  $\bar{P}_{(\cdot)}$  can be identified [25]:

$$\begin{aligned}
 \text{The net power:} \quad \bar{P}_{(a)} &= \frac{1}{T} \int_0^T P(t) dt, \\
 \text{The absolute power:} \quad \bar{P}_{(b)} &= \frac{1}{T} \int_0^T |P(t)| dt, \\
 \text{The positive-only power:} \quad \bar{P}_{(c)} &= \frac{1}{T} \int_0^T P(t) [P(t) \geq 0]_i dt, \\
 \text{The generalised power:} \quad \bar{P}_{(d)} &= \frac{1}{T} \int_0^T (P(t) + Q(t) |P(t)| [P(t) \leq 0]_i) dt,
 \end{aligned} \tag{5}$$

where  $[\cdot]_i$  is the Iverson bracket, with  $[\lambda]_i = 1$  for a true statement  $\lambda$ , and  $[\lambda]_i = 0$  for a false statement  $\lambda$  [101]; and  $Q(t)$  is a general penalty function,  $Q(t) > 0, \forall t$ , penalising negative power. Figure 1C illustrates these metrics on a representative  $P(t)$ . For example, if the actuator can absorb all negative power for later use, i.e. the actuator shows perfect energy regeneration [91, 102], then metric  $\bar{P}_{(a)}$  is appropriate. If the actuation system shows no regeneration, and must expend energy to account for negative power (such as in a rocket reaction engine), then metric  $\bar{P}_{(b)}$  should be used. If the actuation system shows imperfect regeneration, and can dissipate but not store negative power (such as in car brakes), then the relevant metric is  $\bar{P}_{(c)}$ . Different disciplines of study have conventionally used different  $\bar{P}_{(\cdot)}$ . The absolute power is used in robotics [103, 104] and bipedal biomechanics [105–108]; the positive-only power, in insect flight energetics [94, 98, 109]; and the generalised power, in models of human metabolic cost [110–112]. The net power  $\bar{P}_{(a)}$  is independent of the system elasticity,  $F_s(\cdot)$ , because elastic forces are conservative. The question of minimising  $\bar{P}_{(a)}$  with respect to elasticity is thus irrelevant. The net power, absolute power, and positive-only power are particular forms of the generalised power, with constant penalty functions  $Q = 0$ ,  $Q = 2$ , and  $Q = 1$ , respectively.

Fascinatingly, it is possible to devise a solution for the optimal elasticity,  $F_s(\cdot)$ , that is simultaneously valid for all three power consumption metrics,  $\bar{P}_{(b)-(d)}$ . It can be demonstrated that any energy resonant state, i.e. any state in which negative power is absent ( $P(t) \geq 0, \forall t$ ) is necessarily a state in which all of these metrics are simultaneously minimised with respect to elasticity. This solution is given in detail in [25]: it can be derived in what may be described as a three-step

process [25]. *Step 1* is to confirm that the absence of negative power leads to equality among power metrics  $\bar{P}_{(a)-(d)}$ . Intuitively, these metrics penalise negative power flow, and thus, if power flow is non-negative, then these metrics will be equal. *Step 2* is to confirm that the equal metric value in Step 1 is indeed the smallest possible value of metrics  $\bar{P}_{(b)-(d)}$  w.r.t. elasticity,  $F_s(\cdot)$ . Noting, that the net power  $\bar{P}_{(a)}$  is independent of  $F_s(\cdot)$ , and that  $\bar{P}_{(b)-(d)}$  cannot be greater than  $\bar{P}_{(a)}$ , it then follows that if  $\bar{P}_{(a)-(d)}$  are equal then  $\bar{P}_{(b)-(d)}$  are minimised w.r.t. elasticity. *Step 3* is to formulate this minimum in work-loop terms. This process differs between SEA and PEA systems. In PEA systems, for instance, based on the sign of  $\dot{x}$ , we observe that the work loop  $F^\pm(x)$  generates negative power when  $F^+(x) < 0$ , or  $F^-(x) > 0$ . We also observe that  $F_s(x)$  functions as a simple additive between the inelastic and elastic work loops:  $F^\pm(x) = G^\pm(x) + F_s(x)$ , as per Eq. 7. To ensure that  $F^+(x) = G^+(x) + F_s(x) > 0$  everywhere,  $-F_s(x) \leq G^+(x)$  must hold. To ensure that  $F^-(x) < 0$  everywhere,  $-F_s(x) \geq G^-(x)$  must hold. This leads to the following explicit solution for energy resonance, and the energetically optimal elasticity,  $F_s(\cdot)$ :

For PEA systems:

$$G^-(x) \leq -F_s(x) \leq G^+(x), \quad \forall x \in [\min x(t), \max x(t)],$$

For SEA systems:

$$\begin{aligned}
 X^{-'}(F) &\leq -(F_s^{-1})'(F) \leq X^{+'}(F), \quad \forall F \in [\min F(t), 0], \\
 X^{+'}(F) &\leq -(F_s^{-1})'(F) \leq X^{-'}(F), \quad \forall F \in [0, \max F(t)],
 \end{aligned} \tag{6}$$

as illustrated in Fig. 1A and B.  $(\cdot)'$  denotes  $d(\cdot)/dF$ . These are the elastic-bound conditions: they are sufficient conditions on the elasticity,  $F_s(\cdot)$ , to ensure that all three metrics of actuator power consumption are minimised with respect to  $F_s(\cdot)$ ; and are necessary conditions in a wide class of systems [25]. In general, these conditions define not a single optimal elasticity, but a bounded range of optimal elasticities—one of which may be linear, but the rest are nonlinear (Fig. 1A, B). Each optimal elasticity is associated with a particular input load waveform,  $F(t)$ : under this input loading, the system generates the prescribed output response,  $x(t)$ , and operates in energy resonance.

### 2.3 Composite metrics and principles of invariance

The elastic-bound conditions, Eq. 6, define energy resonant states, in  $F_s(\cdot)$ : states which minimise the system mechanical power consumption,  $\bar{P}_{(b)-(d)}$ , at some given state of periodic kinematic output,  $x(t)$ . Significantly, however, these energy resonant states do not *only* optimise  $\bar{P}_{(b)-(d)}$ , but also range of other physically relevant power consumption and performance metrics. The behaviour of some such metrics can be viewed through the lens of two principles of invariance [25]:

#### 2.3.1 First principle of invariance

In any PEA system with periodic kinematic output,  $x(t)$ , the actuator load profile,  $F(t)$  is in general dependent on the system elasticity,  $F_s(\cdot)$ , whereas the actuator displacement profile,  $x(t)$ , is independent of this elasticity—it is prescribed. Hence, any metric which is a functional of solely  $x(t)$  (e.g.  $\max x$ ) is invariant with respect to elasticity. Turning to any SEA system, we observe the reverse: at some given state of periodic kinematic output,  $x(t)$ , the actuator displacement profile,  $u(t)$  is in general dependent on the system elasticity, whereas the actuator load profile,  $F(t)$ , is always independent of this elasticity—it is prescribed by  $F = D(x, \dot{x}, \ddot{x}, \dots)$  (Eq. 2). It follows that in SEA systems, any functional of solely  $F(t)$  is invariant with respect to elasticity. If we define a composite cost metric as a sum of a mechanical power consumption metric ( $\bar{P}_{(b)-(d)}$ ) with *any* other functionals of solely  $F(t)$ , then the only term of this composite cost metric that varies with elasticity,  $F_s(\cdot)$ , is the mechanical power consumption component. The optimal elasticities for this SEA system, in this composite metric, are thus given again by the elastic bound conditions (Eq. 6).

The key relevance of this first principle of invariance, in SEA systems, is that a wide range of practical cost metrics are indeed functionals of solely  $F(t)$  [107]. Equation 7 defines several: the peak load,  $\hat{F}$ , which is a metric of actuator capability requirement; the load-squared metric,  $\bar{P}_{F^2}$ , which is a metric of electrical power consumption [113, 114]; and absolute load metric,  $\bar{P}_{|F|}$ , which is a metric of muscular power consumption [100, 106–108].

$$\begin{aligned} \text{Peak load:} \quad & \hat{F} = \max_t F(t). \\ \text{Load-squared metric:} \quad & \bar{P}_{F^2} = \frac{1}{T} \int_0^T F(t)^2 dt, \\ \text{Absolute load metric:} \quad & \bar{P}_{|F|} = \frac{1}{T} \int_0^T |F(t)| dt. \end{aligned} \quad (7)$$

The first principle of invariance represents an analogy between PEA and SEA systems, and allows the elastic-bound conditions, originally derived for mechanical power minimisation, to be extended to a wider class of optimisation problems.

#### 2.3.2 Second principle of invariance

The first principle of invariance deals with the case in which particular system functions (e.g.  $x(t)$  in a PEA system) are completely independent of elasticity,  $F_s(\cdot)$ . Other functions in these systems (e.g.  $F(t)$  in a PEA system) may be generally dependent on elasticity; but this does not preclude the fact that certain *functionals* of these functions may still be invariant. A key case of this is the absolute load metric,  $\bar{P}_{|F|}$ , in PEA systems. This metric is invariant with respect to elasticities satisfying the elastic-bound conditions (Eq. 6), provided that the prescribed periodic kinematic waveform,  $x(t)$ , is composed of two exactly symmetric curves over its period [25]—that is, provided  $x(t) = x(T - t), \forall t$ . This condition complements the monotonicity analysis condition, i.e. that  $x(t)$  varies monotonically from  $\max(x)$  to  $\min(x)$ ; and monotonically from  $\min(x)$  back to  $\max(x)$ . Nevertheless, these dual conditions are satisfied by many relevant waveforms: simple-harmonic waveforms; triangle-type waveforms, etc. In general,<sup>1</sup> this second principle of invariance means that in PEA systems the elastic-bound conditions, Eq. 6, are also the conditions for an elasticity,  $F_s(\cdot)$ , to be optimal in any combination of mechanical power  $\bar{P}_{(b)-(d)}$  and absolute load ( $\bar{P}_{|F|}$ ). Thus, while in general SEA systems are far superior in optimising useful composite cost metrics, for muscular actuators, PEA systems receive

<sup>1</sup> Indeed, it appears the case that the value of  $\bar{P}_{|F|}$  which is invariant over the elastic-bound region is necessarily the global minimum of  $\bar{P}_{|F|}$  over all possible elasticities—though this point deserves further theoretical treatment.



an unexpected advantage, bringing such systems to nearly the same level of optimality as SEA systems. This has significant implications, for biomimicry: indicating that principles of optimality in muscular systems may not translate to principles of optimality in, for example, electromechanical systems.

### 3 Band-type resonance: theoretical basis

#### 3.1 Definition of band-type resonant states

The formulation of energy resonance outlined in Sect. 2 represents a synthesis of two existing nonlinear analysis strategies: the global resonance analysis of Ma and Zhang [21–24], and the power optimisation approach of Pons and Beatus [20, 25]. Thus far, however, these energy resonant states have been expressed in terms of a set of optimal elasticities,

$F_s(\cdot)$ , that ensure energy resonance for a particular output,  $x(t)$ —rather than the set of inputs/outputs that are energy resonant in a system with fixed elasticity. The non-uniqueness in the set of optimal elasticities gives us reason to pause for a moment: surely, if these optimal elasticities is non-unique, then the input/output energy resonant state should be non-unique? Consider the general 1DOF PEA and SEA systems described in Sect. 2.1, now, with some fixed elastic load profile,  $F_s(\cdot)$ , linear or nonlinear. If, for one such system, some output kinematic waveform,  $x(t)$ , is prescribed, then we may test whether the relevant elastic-bound conditions (Eq. 6) are satisfied—that is, whether this fixed elasticity,  $F_s(\cdot)$ , represents one of the optimal elasticities for  $x(t)$ . If a set of kinematics  $\mathcal{X} = \{x_i(t)\}_i$  exists such that a single  $F_s(\cdot)$  lies within the common bounded work-loop area of  $\mathcal{X}$ , then  $F_s(\cdot)$  is capable of minimising actuator power consumption for the entire set  $\mathcal{X}$ . In this scenario, illustrated in

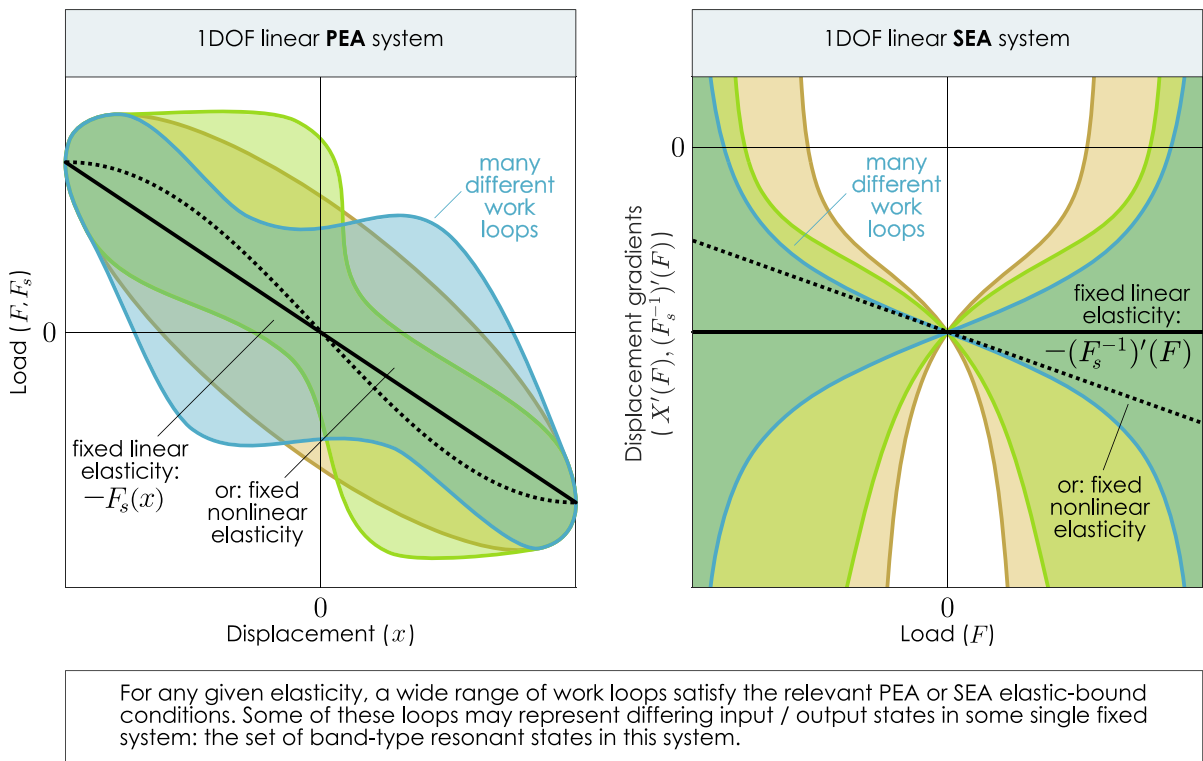


**Fig. 2** Illustration of the principle of band-type resonance. For any given elasticity, the SEA and PEA elastic-bound conditions for energy resonance are satisfied by a wide range of work loops. If, in a single fixed system, we can find multiple kinematic outputs,  $x_i(t)$ , and associated inputs,  $F_i(t)$ ,  $u_i(t)$ , etc., such that the relevant elastic-bound conditions are satisfied, then all of

these input/output states are band-type resonant states in this system: at each state, the overall actuator power consumption is minimised, and is equal to the power consumption of the system's dissipative elements alone—inertia, if present, makes no contribution to overall actuator power consumption

Fig. 2, each  $x_i(t) \in \mathcal{X}$  is associated with specific actuator waveform(s): for PEA systems, the load waveform  $F_i(t)$ ; and for SEA systems, both the displacement  $u_i(t)$  and load  $F_i(t)$  waveforms, which are mutually dependent. All of these states are energy resonant: they contain no negative power ( $P(t) \geq 0$ ,  $\forall t$ ), and thus, ensure that power required to generate each particular  $x_i(t)$  is the minimum possible power required, given any possible choice of system elasticities. By controlling  $u_i(t)$  and/or  $F_i(t)$ , it is possible to switch between output kinematics,  $x_i(t) \in \mathcal{X}$  without leaving energy resonance: the system's fixed elasticity is always energetically optimal for each output.

More formally, consider a general output waveform,  $x(t)$ , parameterised as a functional of period  $T$ , amplitude  $\hat{x}$  and offset,  $x_0$ , and basis waveform  $w(\tau)$  (normalised amplitude, period, and zero mean), in the form  $x(t) = x[\hat{x}, T, x_0, w(\tau), t] = \hat{x}w(t/T) + x_0$ . Note that all of these parameters, including the basis waveform  $w(\tau)$  may vary across the space of states under analysis. This parameterisation is capable of representing all possible variation in periodic  $x(t)$ ; it serves simply to isolate key physically relevant properties (period, peak-to-peak amplitude, etc.) for modulation control. Consider also a PEA system (Eq. 3), with dynamics  $D(x, \dot{x}, \ddot{x}, \dots)$  and fixed  $F_s(x)$ . In this system, the waveform  $x(t)$  generates an inelastic actuator load requirement  $G(t) = D(x, \dot{x}, \ddot{x}, \dots)$ , and an elastic (i.e. overall input) load requirement,  $F(t)$ , via  $F(t) = G(t) + F_s(x(t))$ . The inelastic load requirement,  $G(t)$ , generates a work loop  $G-x$ . This work loop may be parameterised  $G^\pm(x(t))$  if the PEA analysis conditions, (a.i)–(a.iii) in Sect. 2.1, are met: that is, that the work loop associated with  $G(t)$  and  $x(t)$ , in the plane  $G-x$ , is a closed simple curve; no more than bivalued at any  $x$ ; and represents net power dissipation. Now, given  $\hat{x}$ ,  $T$ ,  $x_0$ , and  $w(\tau)$ , and thus given  $x(t)$ , we test if the following condition is true:

$$G^-(x(t)) \leq -F_s(x(t)) \leq G^+(x(t)), \quad \forall t. \quad (8)$$

If this condition is satisfied for the given  $\hat{x}$ ,  $T$ ,  $x_0$ , and  $w(\tau)$ , then the PEA system's fixed elasticity,  $F_s(x)$ , is energetically optimal for the waveform,  $x(t) = x[\hat{x}, T, x_0, w(\tau), t]$ . The set of particular waveforms,  $\mathcal{X} = \{x_i(t)\}_i$ , such that (i) the analysis conditions were met, as per above, and (ii) Eq. 8 is satisfied, we define to be a space of *band-type resonant outputs*

for this specific PEA system (with fixed  $F_s(x)$ , etc.). The set of function tuples,  $\mathcal{S} = \{\{x_i(t), F_i(t)\}\}_i$ , including both particular output waveforms  $x_i(t) \in \mathcal{X}$  and associated input loads  $F_i(t)$ , we define to be the system's set of *band-type resonant states*, as illustrated in Fig. 2.

Alongside, consider an SEA system (Eq. 4), with dynamics  $D(x, \dot{x}, \ddot{x}, \dots)$  and fixed  $F_s(\cdot)$ . In this system, the general waveform  $x(t) = x[\hat{x}, T, x_0, w(\tau), t] = \hat{x}w(t/T) + x_0$  generates a load requirement  $F(t) = D(x, \dot{x}, \ddot{x}, \dots)$ , and an actuator displacement requirement  $u(t) = x(t) + F_s^{-1}(F(t))$ . The load requirement  $F(t)$  generates an inelastic work loop  $x-F$ . This work loop may be parameterised  $X^\pm(F(t))$  if the SEA analysis conditions, (b.i)–(b.iii) in Sect. 2.1, are met: that is, that the work loop associated with  $x(t)$  and  $F(t)$ , in the plane  $x-F$ , is a closed simple curve; no more than bivalued at any  $F$ ; and represents net power dissipation. Given  $\hat{x}$ ,  $T$ , and  $x_0$ , and thus  $x(t)$ , we test the following piecewise condition:

$$\begin{aligned} X^-(F(t)) &\leq -(F_s^{-1})'(F(t)) \leq X^+(F_i(t)), \quad \forall F \in [\min(F(t)), 0], \text{ and} \\ X^+(F(t)) &\leq -(F_s^{-1})'(F(t)) \leq X^-(F_i(t)), \quad \forall F \in [0, \max(F(t))]. \end{aligned} \quad (9)$$

If this piecewise condition is satisfied for the given  $\hat{x}$ ,  $T$ ,  $x_0$ , and  $w(\tau)$ , then the SEA system's fixed elasticity,  $F_s(\cdot)$ , is energetically optimal for the waveform,  $x(t) = x[\hat{x}, T, x_0, w(\tau), t]$ . The set of particular waveforms,  $\mathcal{X} = \{x_i(t)\}_i$ , such that (i) the analysis conditions were met, and (ii) Eq. 9 is satisfied, is defined to be the set of *band-type resonant outputs* for this specific SEA system (again, with fixed  $F_s(x)$ , etc.). The set of function tuples,  $\mathcal{S} = \{\{x_i(t), u_i(t), F_i(t)\}\}_i$ , including particular output waveforms  $x_i(t) \in \mathcal{X}$ , associated input displacements  $u_i(t)$ , and associated input loads  $F_i(t)$ , is this system's set of *band-type resonant states*.

### 3.2 Constructing band-type resonant states

To translate the implicit description of band-type resonant states in Eqs. 8–9 to an explicit description of their input/output waveforms, we observe that these states show a key commonality. The inequalities in Eqs. 8–9 include two equality conditions, or, constraints—points at which the inequality degenerates into equality [25]. In the PEA system, this is the condition for load matching that arises when the

inequality is evaluated at the displacement extrema ( $x(t) = \hat{x} \pm x_0$ ), and in the SEA system, this is the condition for derivative matching that arises when the inequality is evaluated at zero load ( $F = 0$ ):

$$\begin{aligned} \text{PEA: } G^\pm(\hat{x} + x_0) &= -F_s(\hat{x} + x_0), \quad G^\pm(\hat{x} - x_0) = -F_s(\hat{x} - x_0), \\ \text{SEA: } X^\pm(0) &= -(F_s^{-1})'(0). \end{aligned} \quad (10)$$

These conditions are satisfied by all elements of the set of band-type resonant output,  $\mathcal{X}$ , in PEA and SEA systems, respectively. A corollary of this condition is that, if we begin with some initial band-type resonant state,  $x(t) = \hat{x}w(t/T) + x_0 \in \mathcal{X}$ , and then alter only its period ( $T$ ) or offset ( $x_0$ ), then resulting state is not guaranteed to be band-type resonant. For instance, in a linear PEA system, cf. the “Appendix, A.1”, univariate changes to the waveform period,  $T$ , will break load matching (e.g. because the load at the displacement extremum is the peak inertial load, scaling by  $\propto 1/T^2$ ). Univariate changes to the offset  $x_0$  will leave the peak inertial loads invariant, but cause the displacement extrema,  $\hat{x} \pm x_0$ , to shift, altering the values of the elastic load,  $F_s(\hat{x} \pm x_0)$ . Or, more practically stated: in a linear PEA system, if a simple-harmonic input/output waveform is resonant at a particular frequency and zero offset, then this identical waveform will not be resonant at different frequencies, or different offsets. This is precisely the mystery regarding insect flight control—i.e. wingbeat frequency [44, 77] and offset [82, 83] modulation—noted in Sect. 1. The same principle provides the basis for designing band-type resonant states in nonlinear systems: whatever effects are at work, modulating  $x(t)$  so as to maintain constant  $G^\pm(\hat{x} + x_0)$  and  $G^\pm(\hat{x} - x_0)$  (in a PEA system) or constant  $X^\pm(0)$  (in a SEA system) is crucial. The full inequality conditions, Eqs. 8–9, must still be tested on these modulated states; but states satisfying the equality conditions are a necessary prerequisite.

In broad practical terms: given some initial band-type resonant state  $x_1(t) \in \mathcal{X}$ , constructing another different band-type resonant state,  $x_2(t) \in \mathcal{X}$ , requires either varying more than one scalar waveform parameter (amplitude, frequency and offset) and/or varying the basis waveform  $w(\tau)$ . That is, if we desire a set of band-type resonant states, e.g. over a range of different output waveform periods,  $T$ , then one option is to find an associated set of different normalised waveforms,

$w(\tau)$ . This leads to our method for *constructing* band-type resonant states. We first seek a relationship between a scalar waveform parameter (e.g.  $T$ ) and the normalised waveform,  $w(\tau)$ , such that the system-relevant equality condition (Eq. 10) is satisfied over a range of  $T$  (ideally,  $\forall T$ ). This is the process of spectral shaping, and we will describe several analytical and numerical methods for performing it. When we have obtained this relationship, we then assess whether these  $\{T, w(\tau)\}$  tuples satisfy the system-relevant inequality condition, Eq. 8 or Eq. 9. We find, by nature of their inequality, that these conditions are satisfied within a certain range (or band) of  $T$ . Performing this with  $T_i$  and  $w_i$ , we obtain *frequency-band resonance*: energy resonance over a band of frequencies. Performing this with  $\hat{x}$ ,  $x_0$  (in some combination) and  $w_i$ , we obtain *offset-band resonance*: energy resonance over a band of offset parameters.

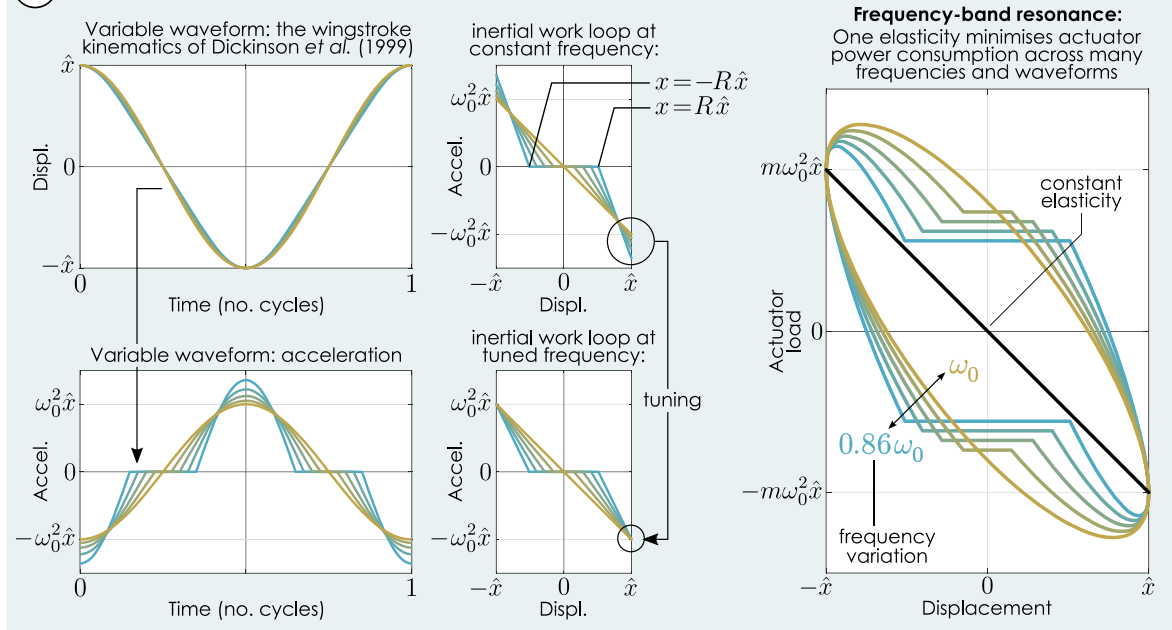
Among the huge space of possible band-type resonant effects, frequency-band and offset-band resonance are the two cases that we demonstrate in detail below. These particular cases have significant relevance to many practical systems—including several forms of biomimetic propulsion system. They allow frequency (i.e. thrust magnitude) and offset (i.e. thrust-vectoring) control, while maintaining resonant power optimality. We will demonstrate three different techniques for spectral shaping (obtaining a relationship, e.g. between  $T_i$  and  $w_i$ ) that satisfy the system-relevant inequality condition: analytically tuning a generative ordinary-differential equation (ODE); analytically tuning a multiharmonic waveform; and numerically tuning a multiharmonic waveform.

## 4 Band-type resonance: applications

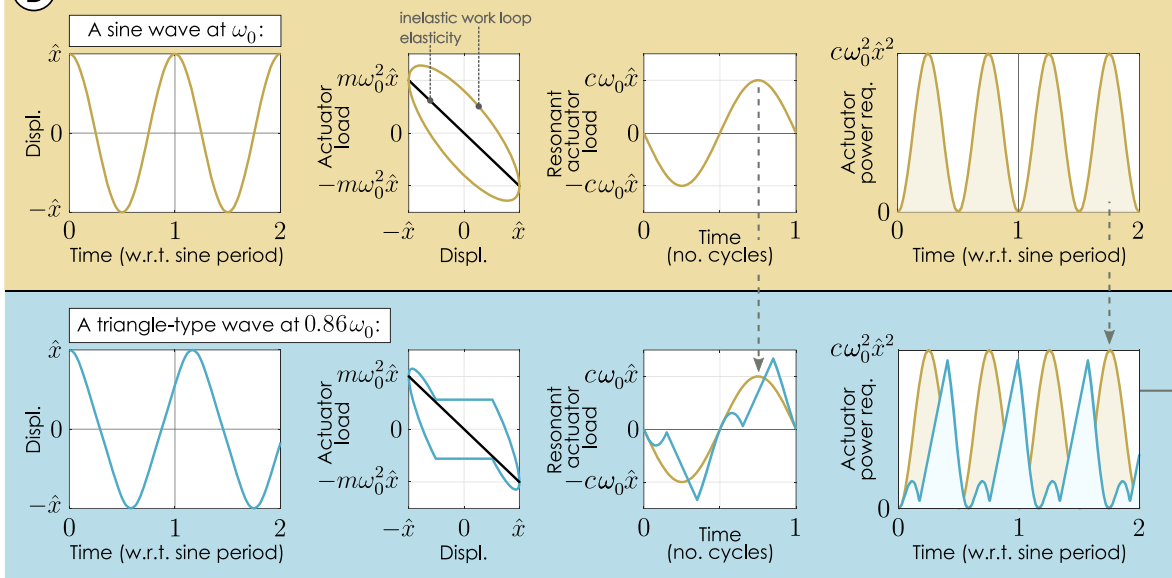
### 4.1 Frequency-band resonance in a PEA system, via analytical tuning of a generative ordinary-differential equation (ODE)

As a specific demonstration of frequency-band resonance, consider a 1DOF PEA system (Fig. 1) with fixed linear inertia, linear dissipation, and linear elasticity:

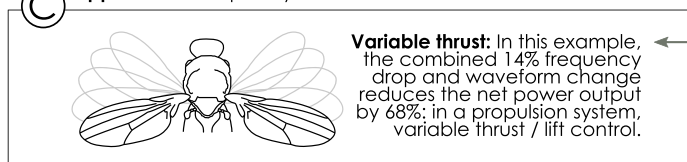
### A Frequency-band resonance in a PEA system, via analytical tuning of a generative ODE



### B Example: Two frequencies, two waveforms: both energetically optimal:



### C Application: Frequency-modulated control



◀ **Fig. 3** Frequency-band resonance in a PEA system, via analytical tuning of a generative ordinary-differential equation (ODE). **A** Frequency-band resonance in a PEA system. For demonstration, we utilise a generalisation of the triangle-like waveform of Dickinson et al. [95], devised as a model of insect wing-stroke kinematics; and a linear PEA system. At a constant fundamental frequency ( $\omega_0$ ) the peak accelerations for each waveform does not match; the fundamental frequency must be tuned to generate a match. When this is done, the work loops for a range of waveforms show a common optimal linear elasticity—that is, optimal resonant power savings are available at a range of frequencies and waveforms. **B** For further demonstration, two specific frequency-band resonant states are detailed: a sine waveform at reference frequency  $\omega_0$ , and a triangle-like waveform at frequency  $0.86 \omega_0$ ; the extremal cases. The modulation in resonant load and power waveform for each are illustrated—note the absence of negative power in both cases. **C** An example application: frequency-modulated thrust or lift control in biomimetic propulsion systems, at optimal mechanical efficiency

Inelastic system dynamics:	$D(\dot{x}, \ddot{x}) = m\ddot{x} + c\dot{x} \ (m > 0, c > 0).$
Inelastic load requirement:	$G(t) = D(\dot{x}, \ddot{x}) = m\ddot{x} + c\dot{x}.$
Fixed elasticity:	$F_s(x) = kx, \ (k > 0).$
Elastic load requirement:	$F(t) = G(t) + F_s(x) = m\ddot{x} + c\dot{x} + kx.$
Natural frequency:	$\omega_0 = \sqrt{k/m}.$
Damping ratio:	$\zeta = c/2\sqrt{km}.$

(11)

This linear PEA system can be used as a simple model of insect flight motors [20, 45], low-Reynolds number propulsion systems [115], and MEMS devices under electrostatic forcing [27]. In all of these systems, periodic outputs composed of two monotonic curves, as per analysis condition (a.ii) in Sect. 2.1 are directly relevant to system operation: as propulsive kinematics [95, 116] or detection kinematics in MEMS sensors [27]. To demonstrate frequency-band resonance in this system, via an analytical spectral shaping process, we use a triangle-like waveform based on that used by Dickinson et al. [95] and experimentally verified by others [116] as a model of the wing stroke-angle kinematics in fruit flies. This waveform consists of constant velocity sections, as in a triangle wave, connected by sinusoid segments at the points of velocity reversal. When this waveform is visualised in the  $\ddot{x}$ - $x$  space, it appears as a freeplay nonlinearity (Fig. 3A). As such, it can be generated as the solution of an additional ordinary-differential equation (ODE), controlled by a sharpness parameter  $R$ :

$$\ddot{x} = h(x) = \begin{cases} -\omega^2 K(R)(x + R\hat{x}) & -\hat{x} \leq x \leq -R\hat{x} \\ 0 & -R\hat{x} \leq x \leq R\hat{x} \\ -\omega^2 K(R)(x - R\hat{x}) & R\hat{x} \leq x \leq \hat{x} \end{cases}$$

$$K(R) = \left( \frac{2R}{\pi(1-R)} + 1 \right)^2$$

 Initial conditions:  $\dot{x}(t=0) = 0, x(t=0) = \hat{x}$ .

(12)

The solution,  $x(t)$ , to this generative free-play, nonlinear, ODE is the desired parameterised triangle-like waveform. The ODE parameters are the waveform amplitude  $\hat{x}$ , angular frequency  $\omega$ , and the sharpness parameter  $0 \leq R < 1$ . The latter represents the width of the freeplay region in  $\ddot{x}$ - $x$  space: in the time-domain, the region of constant velocity. The other region, where  $\ddot{x} \propto -x$ , generates sinusoidal segments that interpolate between these regions of constant velocity. Setting  $R = 0$  generates a pure sinusoid; and  $R \rightarrow 1$  a pure triangle wave. Further details of the waveform formulation in the time domain are given in the “Appendix A.2”.

Note that this generative ODE approach is applicable to a wide range of other systems and waveforms: its key feature is that, instead of parameterising waveforms in the time domain, we parameterise them in the domain  $\ddot{x}$ - $x$ , as solutions of an ODE of the form  $\ddot{x} = h(x)$ . The reason for parameterising waveforms in this plane is that the resulting function  $h(x)$  be directly represented on the work loop of a system with linear inertia, as  $\ddot{x} = h(x)$  (Fig. 3A). In addition, the formulation in  $h(x)$  allows us to encapsulate complex waveform dependencies (e.g. involving of an infinite series of harmonics in the time domain) with a closed-form expression. The disadvantage is that computing the associated time-domain waveforms may be non-trivial: numerical methods may be required. Together, these properties lend the generative ODE approach significant utility as a theoretical tool; but make it less well-suited for the design of real-time control algorithms for band-type resonant states.

As an illustration of this, consider our linear PEA system (Eq. 11). We start at a prescribed linear resonant state: a simple-harmonic waveform ( $x_0(t)$ ,  $R = 0$ ) at the natural frequency  $\omega_0$ , and any amplitude,  $\hat{x}_0$ . By the elastic-bound condition (Eq. 8), we can confirm that this state is energy resonant ( $x_0(t) \in \mathcal{X}$ ). If we then alter the prescribed output waveform from



$x_0(t)$  to  $x_R(t)$ , maintaining constant  $\omega = \omega_0$  and  $\hat{x} = \hat{x}_0$ , but altering  $R$  to some  $R > 0$ , then the resulting  $x_R(t)$  no longer satisfies the PEA equality conditions (Eq. 10). Namely, the loads at the displacement extrema do not remain constant:

$$\begin{aligned} \text{For } x_0(t) : \text{e.g., } G^\pm(\hat{x}_0) &= mh(\hat{x}_0) = -m\omega_0^2\hat{x}_0. \\ \text{For } x_R(t) : \text{e.g., } G^\pm(\hat{x}_0) &= mh(\hat{x}_0) \\ &= -m\omega_0^2K(R)(1-R)\hat{x}_0 \neq -m\omega_0^2\hat{x}_0, \end{aligned} \quad (13)$$

$x_R(t)$  is thus not energy resonant ( $x_R(t) \notin \mathcal{X}$ ). To ensure at least that the PEA equality conditions (Eq. 10) are satisfied, starting again from  $x_0(t)$ , we alter  $\omega$  and  $R$  simultaneously, and use our generative ODE (Eq. 12) to obtain a new waveform,  $x_{R,\omega}(t)$ . For this waveform, at general  $R$  and  $\omega$ , the loads at the displacement extrema are:

$$\begin{aligned} G^\pm(\hat{x}_0) &= mh(\hat{x}_0) = -m\omega^2K(R)(1-R)\hat{x}_0 \\ &= -G^\pm(-\hat{x}_0). \end{aligned} \quad (14)$$

Thus, so ensure these loads (Eq. 14) are equivalent to the linear resonant loads (Eq. 13), we require that, at any  $R$ , the frequency is determined by  $\omega = \Omega(R)$ , where:

$$\Omega(R) = \frac{1}{\sqrt{(1-R)K(R)}}\omega_0. \quad (15)$$

Note that  $\Omega(R) \leq \omega_0$ ,  $\forall R$ . Equation 15 is an analytical tuning relation, generating a continuous set of tuned waveforms,  $x_{R,\Omega(R)}(t)$ , of varying frequency and sharpness, and satisfying the PEA equality conditions (Eq. 10).

We then compute the range of  $R$  for which  $x_{R,\Omega(R)}(t) \in \mathcal{X}$ : that is,  $R$  for which the tuned waveforms,  $x_{R,\Omega(R)}(t)$  satisfy the full PEA elastic-bound inequality conditions, and are thus energy resonant. We observe that  $x_{R,\Omega(R)}(t)$  satisfying these inequality conditions, satisfy them over the range  $0 \leq R \leq R^*$ , for some critical  $R^* \geq 0$ . This range yields a frequency range  $\omega^* \leq \omega \leq \omega_0$ , for some critical  $\omega^* = \Omega(R^*)$ . It is possible to compute  $R^*$  analytically, under the observation (cf. Figure 3A) that the violation of the PEA inequality condition, i.e. the intersection of  $-F_s(x)$  and  $G^\pm(x)$ , always occurs first at  $x = \pm R^*\hat{x}$ . Solving for  $R^*$  in  $-F_s(R^*\hat{x}) = G^\pm(R^*\hat{x})$  yields the critical values:

$$\begin{aligned} R^* &= \frac{-c^2 + c\sqrt{c^2 + 4m^2\omega_0^2}}{2m^2\omega_0^2} = -2\zeta^2 + 2\zeta\sqrt{1 + \zeta^2}. \\ \omega^* &= \Omega(R^*) = \frac{1}{\sqrt{(1-R^*)K(R^*)}}. \end{aligned} \quad (16)$$

The tuned waveform generated by Eq. 12 is energy resonant for this PEA system over the entire range  $0 \leq R \leq R^*$ ,  $\omega = \Omega(R)$ ,  $\omega^* \leq \omega \leq \omega_0$ , and for  $\hat{x} = \hat{x}_0$ . The associated input load requirement is the associated  $F(t)$  given in Eq. 11.

Figure 3A illustrates this process graphically. The system dimensional parameters are,  $m = 1$ ,  $c = 0.8$ ,  $k = 1$ ; or, as an equivalent canonical oscillator,  $\omega_0 = 1$  and damping ratio  $\zeta = 0.4$ . We prescribe oscillations with amplitude  $\hat{x} = \hat{x}_0 = 1$ . Under these conditions, the analytical results for the critical waveform parameters are  $R^* \cong 0.54$  and  $\omega^* \cong 0.84 \omega_0$ . A graphical approach confirms these values: we can easily obtain a conservative estimate for  $R^*$  by incrementing  $R$  over  $0 \leq R < 1$  and observing when there is an intersection between the inelastic work loop,  $G(t)-x(t)$ , and the linear elasticity  $F_s(x)$ . Using this approach, we estimate  $R^* \cong 0.51$  and  $\omega^* \cong 0.86 \omega_0$ , as illustrated in Fig. 3A. Thus, we have obtained frequency-band resonance: output waveforms with  $0 \leq R \leq 0.51$  are energy resonant, and span a range of frequencies,  $0.86 \omega_0 \leq \omega \leq \omega_0$ . This range of frequencies is specific to this particular PEA system, and the choice of the triangle-type variable waveform (Eq. 12). This range is not, in fact, the widest range available for this particular system under *any* possible variable waveform. Heuristically, we may observe that a wider range of frequencies would be available if we used different waveforms generated by smoother acceleration functions in the generative ODE, for instance,  $\ddot{x} \propto -x^3$ . There, the curve  $x^3$  describes the inertial component of the inelastic work loop ( $G-x$ ), i.e. the midline of  $G^\pm(x)$ . Geometrically, a midline with strong changes in derivative, i.e. pronounced peaks, will allow smaller changes in frequency, before  $G^\pm(x)$  intersects the elasticity,  $F_s(x)$ , violating the elastic-bound condition (Fig. 3A). A smoother midline will, instead, delay condition violation, and is thus preferable.

These results are intriguing. Even in a perfectly linear system, by using relatively small changes in waveform (Fig. 3A), we can change the frequency of the system output, within a certain band, and still

maintain perfect energy transfer, i.e. minimum overall actuator power consumption for the associated output. At each of these frequencies and waveforms, the fixed system elasticity is energetically optimal: it is impossible to decrease the actuator mechanical power consumption, under any metric (Sect. 2.2), by choosing any other elasticity. Note that, in this examples PEA system with linear inertia and dissipation, this minimum power consumption is equivalent to the power consumption of the dissipative element alone—in intuitive terms, inertial effects are absorbed by elastic effects. In this example PEA system and waveform, we can alter<sup>2</sup> the output frequency by up to 14% of the initial fundamental frequency, corresponding to a 32% modulation in the net power flow through the system, while maintaining energetic optimality. Consider an application of this principle in a biomimetic vibrational propulsion system: this frequency modulation capability could represent continuous lift or thrust control, or the operation of a propulsion system at two distinct frequencies (Fig. 3B, C). For instance, we might select two extreme frequency-band states as two modes of operation for a MEMS micro-swimmer robot: a simple-harmonic response at  $\omega_0$ , and a frequency-band resonant response at  $0.86 \omega_0$ . One fixed elasticity would allow energetically optimal operation at both frequencies, providing us with two propulsive modes, high-thrust and low-thrust. Indeed, the linear energy resonant states presented in this section are particularly relevant to micro-swimmer robots, for which dissipative forces may be linear (Eq. 11) [117].

We can extend this concept further, by contemplating the possibility of continuously passing a system through frequency-band resonant states, and thus, continuously modulating the system operating frequency. In an insect, or an FW-MAV, this would represent continuous lift control via frequency modulation, at a state of continuous energetic optimality—

<sup>2</sup> A technical point: in this PEA system, a triangle-type waveform defined by Eq. 12 allows only a reduction in frequency relative to the initial simple-harmonic waveform. Obtaining an increase in frequency is relatively simple. We can (i) define the initial state as multiharmonic ( $R \neq 0$ ) instead of single-harmonic ( $R = 0$ ), or (ii) choose an alternative generative ODE,  $\ddot{x} = h(x)$ : e.g.,  $h(x) \propto -\text{sgn}x|x|^n$ ,  $0 < n \leq 1$ , which generates increases in frequency over a sine wave ( $n = 1$ ). There is scope for a theoretical treatment of the relationship between  $h(x)$  and the frequency-band resonant states it generates—we leave such a treatment to future work.

a novel form of control, which is consistent with similar control behaviour observed in insects. Honeybees, fruit flies, and hawkmoths are observed to modulate wingbeat frequency as a mechanism of aerodynamic force control [44, 77–79]; mosquitos are observed to do so in acoustic courtship interactions [90, 118]; and many species of bee and fly show temperature-dependent wingbeat frequency variation that is thought to be a form of internal temperature regulation [80, 119]. Quantitatively, the linear model studied in Fig. 3, with  $\zeta = 0.4$ , is a broad approximation of a strongly damped insect, e.g. a fruit fly [20]. Fruit flies have been observed to show wingbeat frequency modulation of up to 15%; a value consistent with our estimate of 14% modulation under continual energetic optimality. Frequency-band resonance may indeed provide an explanation for this biological control behaviour—an explanation which is valid for both linear and nonlinear models of the insect flight motor.

In addition, frequency-band resonance may provide insight into the nominal operating state of biological propulsion systems, such as insect flight motors. Given that insect wing stroke kinematics in steady level flight are not exactly simple-harmonic [94, 95, 116, 120], frequency-band resonance implies that the energy resonant state of the real flight motor may *not* be at the same frequency as the simple-harmonic energy

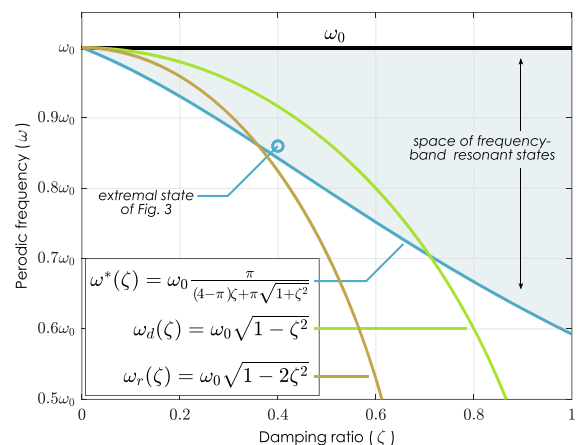
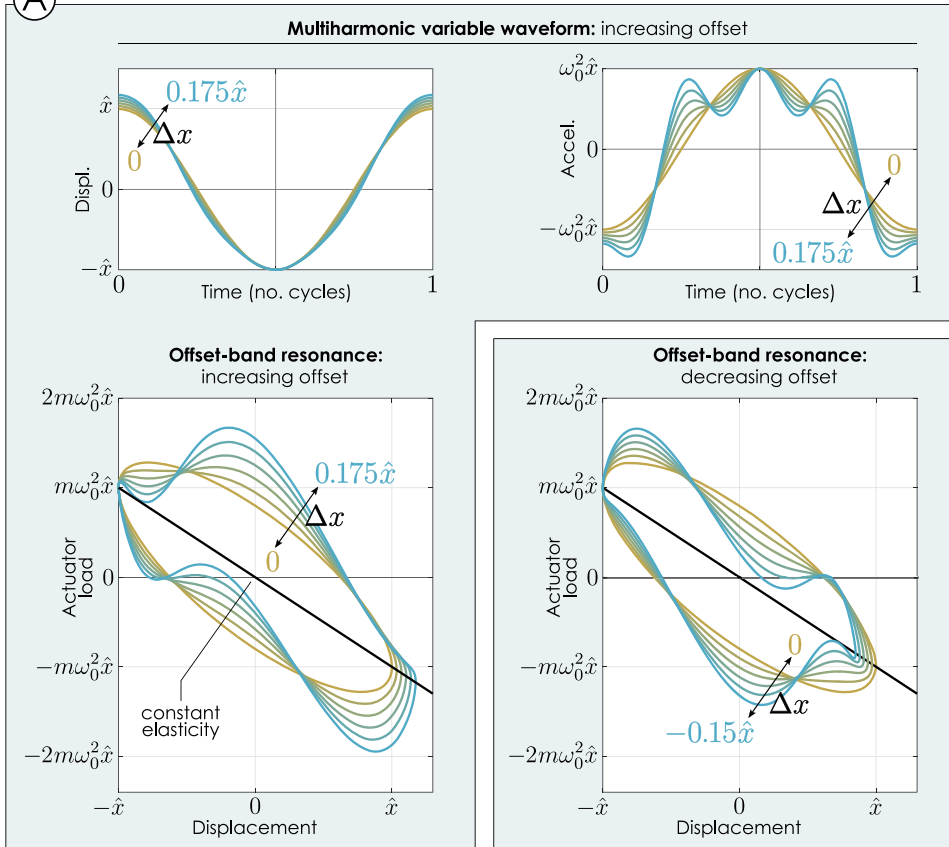
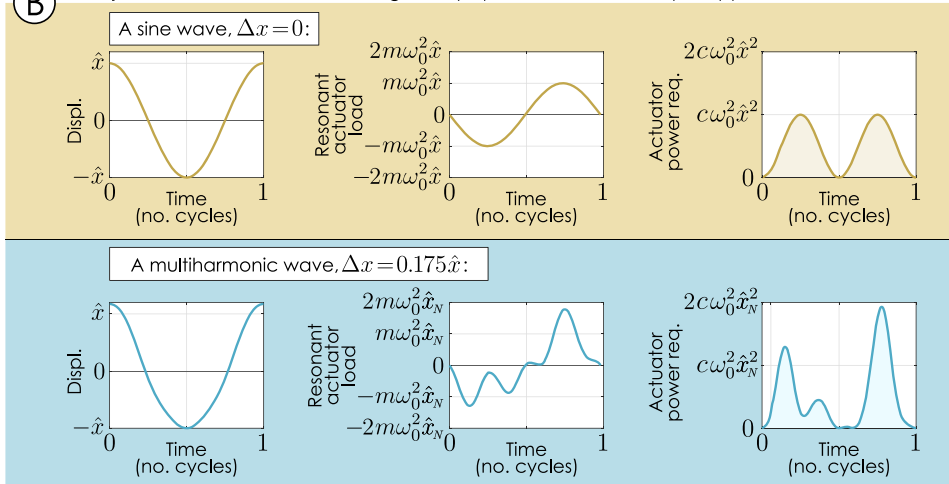


**Fig. 4** The critical frequency and three classical frequencies, as function of damping ratio. The critical frequency,  $\omega^*$ , is the lower bound of the space of frequency-band resonant states (in  $R$ ), i.e. the minimum frequency for which an energy resonant state exists at some waveform. In a linear system, it is distinct from the three classical frequencies—the natural frequency,  $\omega_0$ ; damped natural frequency,  $\omega_d(\zeta)$ ; and simple-harmonic resonant frequency,  $\omega_r(\zeta)$ —but is of similar magnitude

### (A) Offset-band resonance in a PEA system



### (B) Example: Two waveforms: both energetically optimal; and an example application



### (C)

**Application:** Vectored-thrust control in propulsion systems. Offset variation allows the alteration of the direction associated with propulsive thrust, e.g., lift in an insect, or FW-MAV system.

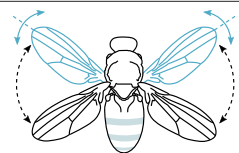


**Fig. 5** Offset-band resonance in a PEA system. **A** Offset-band resonance in a PEA system. For demonstration, we utilise a multiharmonic waveform as per Eq. 17; and a linear PEA system. By default, this multiharmonic waveform satisfies the condition for acceleration-matching at the displacement extrema ( $-\hat{x}$  and  $\hat{x} + \Delta x$ ); and thus, the work loops for a range of waveforms show a common optimal linear elasticity—optimal resonant power savings are available at a range of single-point offsets ( $\Delta x$ ), both positive and negative. **B** For further demonstration, two specific offset-band resonant states are detailed: a simple-harmonic waveform, and a multiharmonic waveform at  $\Delta x = 0.175 \hat{x}$ ; the positive extremal case. The modulation in resonant load and power waveform are illustrated—note the continued absence of negative power. **C** An example application: vectored-thrust control in propulsion systems, e.g. FW-MAVs

resonant state (i.e.  $\Omega(R) \leq \omega_0$ , Eq. 15). For instance, consider modelling a flight motor as a strongly damped PEA system with linear elasticity, and with wingbeat kinematics,  $x(t)$ , described by a waveform with nonzero sharpness parameter—e.g.  $R \approx 0.6$  [95, 120]. The frequency at which these wingbeat kinematics are most efficiently generated, in terms of minimum power consumption, is lower than the flight motor natural frequency:  $\Omega(R) < \omega_0$ . For  $R \approx 0.6$ , we can estimate  $\Omega(R) \approx 0.80 \omega_0$ . This is an approximate estimate, based on linear, and purely parallel, elasticity.

To gain a broader understanding of this effect, we can examine the critical frequency and sharpness,  $\omega^*$  and  $R^*$  (Eq. 16), of our linear PEA model, as a function of the structural damping ratio,  $\zeta$ . This puts loose bounds on the maximum possible waveform sharpness, and minimum waveform energy resonant frequency, of a simple PEA system—for instance, a model of an insect flight motor. Figure 4 shows an illustration of these bounds, tracking the critical frequency,  $\omega^*(\zeta)$ , over  $\zeta$ , alongside the three classical frequencies: the undamped natural frequency,  $\omega_0$ ; the damped natural frequency,  $\omega_d(\zeta)$ ; and the simple-harmonic resonant frequency,  $\omega_r(\zeta)$  [121]. Several interesting points can be noted. (i) The band-width of the frequency-band states increases with damping, approximately linearly. (ii) These specific results provide some basic properties of the extrema of the set of band-type resonant outputs,  $\mathcal{X}$ , in this linear PEA system. For one, the element of  $\mathcal{X}$  with the lowest frequency,  $\omega$ , and a triangle-wave waveform (Eq. 12), has frequency  $\omega = \omega^*$  as defined in Eq. 16 and plotted

in Fig. 4. This implies that the element of  $\mathcal{X}$  with the lowest frequency has frequency at least as low as this  $\omega^*$ —an upper bound on the lowest frequency. There is significant potential for further analysis to determine more detailed properties of  $\mathcal{X}$  (e.g. the exact extremal frequencies in this linear system, and these frequencies in different systems). (iii) In the case of an insect flight motor, these effects could explain discrepancies between measured motor natural frequencies and insect wingbeat frequencies [42]. Based on the relationship between damping ratio and  $Q$ -factor,  $\zeta \approx 1/2Q$  [20, 122], and existing estimates of the  $Q$ -factor for insect flight [20, 45], we would estimate  $0.3 \leq \zeta \leq 0.4$  for a wide range of insect species. This would correspond to a frequency drop of 10–15% with respect to the natural frequency, which is a significant proportion of the frequency mismatch observed in [42]. And finally, (iv) This analysis can be repeated for more accurate models of insect flight motors, e.g. with quadratic damping, computational models of fluid–structure–interaction, or experimental similitude models. Such analyses would yield more accurate estimates of the explanatory power of frequency-band resonance in insects, and its potential capability in FW-MAVs. The principles of frequency-band resonance that we have studied in this system transfer directly to nonlinear PEA systems (Sects. 3.1–3.2), for which numerical analysis techniques may be more practical, as demonstrated in Sect. 4.3. Applications for frequency-band resonance in nonlinear systems form a broad constellation of possibilities, which we have only just begun to observe.

#### 4.2 Offset-band resonance in a PEA system, via analytical spectral tuning

In the same system used in Sect. 4.1—a general time-invariant 1DOF linear system, under PEA, with fixed inertia, dissipation, and elasticity—we find also the phenomenon of offset-band resonance. Within the set of band-type resonant states for this system, there are not only symmetric states at different frequencies (frequency-band resonance), but, in addition, symmetry-broken states: states with non-symmetric output,  $x(t)$ . As a test case, we focus on a form of offset-band resonance that is directly relevant to insect flight (Fig. 5): the case where one extremum of the output waveform is held fixed (constant  $\min x$ ) and the other is modulated (variable  $\max x$ ). This asymmetry

modulation corresponds to a form of insect body pitch control: symmetric modulation of only the forward-stroke position of the two wings [82, 83]. Here, we illustrate an approach for constructing these offset-band resonant states based on analytically tuning a multiharmonic waveform—a method particularly relevant to control applications. Beginning with a simple-harmonic waveform,  $x(t) = \hat{x}\cos(\omega_0 t)$ , at the system linear resonant frequency,  $\omega_0$ , and some initial amplitude,  $\hat{x}$ , we desire an extension into asymmetric amplitudes ( $\max x \neq -\min x$ ), such that: (i) the displacement minimum is constant ( $\min x = -\hat{x}$ ), and the displacement maximum is modulated by some  $\Delta x$  ( $\max x = \hat{x} + \Delta x$ ); and (ii) the PEA equality conditions (Eq. 10) are satisfied.

As a candidate for such a waveform, we select a multiharmonic waveform, with fundamental period  $T_0 = 2\pi/\omega_0$ , and containing cosine terms of even order (to ensure symmetry about  $t = T_0/2$ ):

$$x(t) = a_1 \cos(\omega_0 t) + a_2 \cos(2\omega_0 t) + a_4 \cos(4\omega_0 t). \quad (17)$$

The intuition behind this particular choice is that even harmonics,  $\cos(n\omega t)$  with  $n$  even, alter the waveform extrema asymmetrically, and therefore are well-suited to offset-band resonance. We will need one fundamental harmonic ( $\omega_0$ ); one harmonic ( $2\omega_0$ ) just to ensure modulation of  $\max x$  independent of  $\min x$ ; and at least one additional harmonic ( $4\omega_0$ ) to satisfy the PEA equality condition. To compute appropriate coefficients,  $a_1$ ,  $a_2$  and  $a_3$ , we define conditions for the two cycle extrema at  $t = 0$  and  $t = T_0/2$ :

$$\begin{aligned} \text{Displacement extrema:} \quad & x(0) = \hat{x} + \Delta x, \\ \text{PEA equality conditions:} \quad & \ddot{x}(0) = -\omega_0^2(\hat{x} + \Delta x), \end{aligned}$$

an expression which is obtained by substituting Eq. 18 into Eq. 17 and solving for  $a_1$ ,  $a_2$  and  $a_3$ . Equation 19 is variable waveform parametrised by,  $\Delta x$ . Under certain conditions on  $\Delta x$ , this waveform will simultaneously generate the appropriate waveform kinematic change ( $\min x = -\hat{x}$ ,  $\max x = \hat{x} + \Delta x$ ) and satisfy the PEA equality conditions.

The conditions on this solution that we must be mindful of are as follows. (i) In defining acceleration conditions at  $t = 0, T_0/2$ , we have assumed that these times correspond to the displacement extrema:  $\max x = x(0)$  and  $\min x = x(T_0/2)$ . We expect that this assumption will hold true over a certain range of coefficient values ( $a_1$ ,  $a_2$  and  $a_3$ ): in particular, it will hold true when the fundamental harmonic is dominant ( $a_1 \gg a_2, a_3$ ). (ii) However, as per Sect. 2.1, the conditions of our PEA system analysis specify that  $x(t)$  must be composed of two monotonic curves over its period: it must vary monotonically from  $\max(x)$  to  $\min(x)$ ; and monotonically from  $\min(x)$  back to  $\max(x)$ . That is,  $\Delta x$  must be such that  $\dot{x}(t) = 0$  only at  $t = 0$  and  $t = T_0/2$ . The latter is a more restrictive condition than the former: if condition (i) fails, then condition (ii) necessarily fails, but not vice-versa. The limits on the available  $\Delta x$  interval—such that Eq. 18 is admissible under our analysis, and satisfied the PEA equality conditions—are thus defined by condition (ii). Analytical approaches to computing these limits are unwieldy: we provide a conservative numerical estimate:  $-0.4 < \Delta x/\hat{x} < 0.7$  for condition (ii) to be satisfied. Note that this interval is specific to this particular waveform (Eq. 19), and is not a property of band-type resonance in this system generally.

$$\begin{aligned} x(T_0/2) &= -\hat{x}, \\ \ddot{x}(T_0/2) &= \omega_0^2 \hat{x}. \end{aligned} \quad (18)$$

That is, the acceleration  $\ddot{x}(T_0/2)$  is independent of  $\Delta x$  whereas the acceleration  $\ddot{x}(0)$  scales linearly with  $\Delta x$ , starting from  $\omega_0^2 \hat{x}$  (Fig. 5). The waveform that satisfies Eqs. 17–18 is:

$$\begin{aligned} x(t) = & \left( \hat{x} + \frac{1}{2} \Delta x \right) \cos(\omega_0 t) + \frac{5}{8} \Delta x \cos(2\omega_0 t) \\ & - \frac{1}{8} \Delta x \cos(4\omega_0 t), \end{aligned} \quad (19)$$

Finally, the interval in  $\Delta x$  that we have just defined is only the interval such that  $x(t)$ , as per Eq. 19, is admissible under our analysis, and satisfies the PEA equality conditions (Eq. 10). The full PEA *inequality* conditions (Eq. 8) may be satisfied only over some subinterval of this interval (possibly, nowhere). This subinterval is the set of offset-band resonant outputs. We estimate it numerically and graphically (Fig. 5) as



– 0.15 <  $\Delta x/\hat{x}$  < 0.175 (Fig. 5). That is, a 17.5% increase, and 15% decrease in the displacement at the full-cycle point (max $x$ ) are available, at continuous power optimality, and at an output waveform which shows only small deviations from a simple-harmonic waveform (Fig. 5).

In vibrational propulsion systems, such as FW-MAVs [56] and micro-swimmers [115], asymmetry modulation is of key importance. In these systems, offset-band resonance could allow resonant thrust-vectoring: position and orientation control via modulation of the distribution of lift, thrust, and other propulsive forces in space and time [82, 123]. For instance, the particular form of offset control studied in this section is identical to that used by fruit flies for pitch-axis control [82, 83]. The offset ( $\Delta x$ ) modulation reported by Whitehead et al. [82] for fruit flies lies within the range – 0.4 <  $\Delta x/\hat{x}$  < 0.4. Our predicted frequency-band range for a broadly representative fruit fly flight motor, with  $\zeta = 0.4$ , explains just under half of this reported offset modulation range—at the least, significantly alleviating the energetic cost of this control modulation behaviour. In FW-MAV systems, a sufficient characterisation of the system stability and controllability may allow the development of a similar pitch-axis continuous controller based on offset-band resonance. Indeed, in continuous-control applications, the multiharmonic approach to generating these offset-band states may have a significant advantage over the generative ODE approach (Sect. 4.2): the control space in actuator load is simple and easily accessible. That is, the only control parameters required are the components of the actuator load at frequencies  $\omega_0$ ,  $2\omega_0$ , and  $4\omega_0$ . And finally, we note that a wide range of other forms of offset-band phenomena are also available using only a few harmonics: for instance, the symmetric waveform shift from  $x \in [-\hat{x}, \hat{x}]$  to  $x \in [-\hat{x} + \Delta x, \hat{x} + \Delta x]$ . This symmetric shift may be particularly relevant to applications requiring less coupling between thrust and steering [124]: unlike the biomimetic single-point control studied in this section, the symmetric shift maintains a more constant overall power output (e.g. a more constant lift force in a FW-MAV).

#### 4.3 Frequency-band resonance in an SEA system, via numerical spectral tuning

As per Sect. 3.1, band-type resonance is also available in SEA systems. The multiharmonic approach

introduced in Sect. 4.2 is a suitable methodology for constructing these band-type resonant states, and is demonstrated here as a numerical approach. For SEA frequency-band resonance, we select the following parametrised waveform:

$$x(t) = \hat{x}(1 - \alpha(\omega)) \cos(\omega t) + \hat{x}\alpha(\omega) \cos(3\omega t), \quad (20)$$

with constant amplitude  $\hat{x}$ ; frequency  $\omega$ , which will be modulated; and a tuning function  $\alpha(\omega)$ . The intuition behind this choice of harmonic is that odd harmonics,  $\cos(n\omega t)$  with  $n$  odd, alter the waveform extrema symmetrically, and are therefore well-suited for frequency-band resonance. As the magnitude of a single harmonic can be tuned to the frequency (Eq. 20), we typically require only one odd harmonic for frequency-band resonance. Given that symmetry is preserved, tuning frequency-band resonance is typically easier than offset-band resonance—to the extent that we can devise a robust numerical method for this process, as follows.

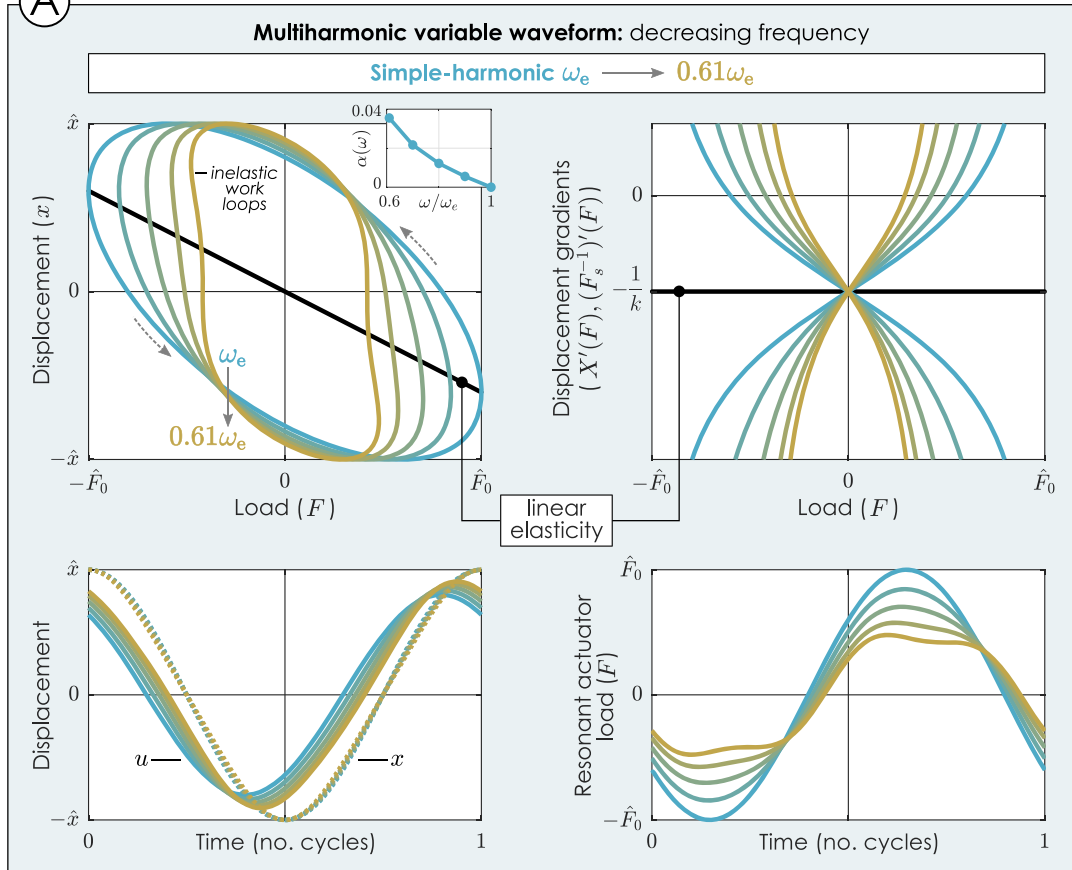
Consider a linear SEA system:

System dynamics:	$D(\dot{x}, \ddot{x}) = m\ddot{x} + c\dot{x}$ .
Load requirement:	$F(t) = D(\dot{x}, \ddot{x}) = m\ddot{x} + c\dot{x}$ .
Fixed elasticity:	$F_s(u - x) = k(u - x)$ .
Natural frequency:	$\omega_0 = \sqrt{k/m}$ .
Damping ratio:	$\zeta = c/2\sqrt{km}$ .
Energy resonant frequency:	$\omega_e = \omega_0\sqrt{1 - 4\zeta^2}$ .

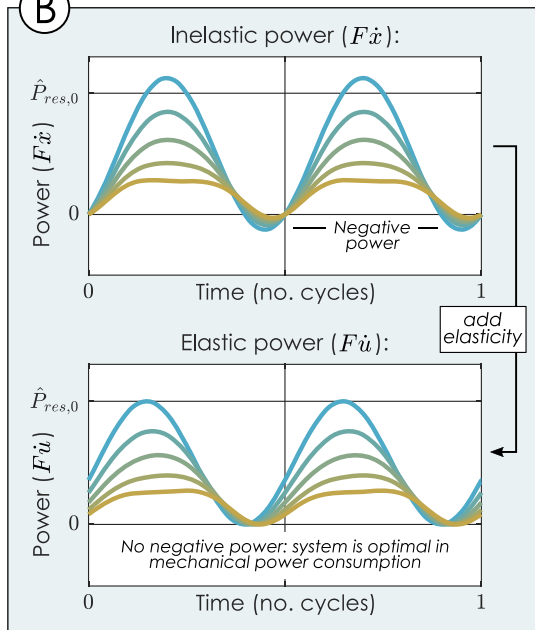
(21)

This linear SEA system can be used as a simple model of MEMS systems under base-excitation [27]; atomic force microscopes [32, 33]; certain insect flight motors [20, 45]; and prosthetic and robotic leg structures [61, 62]. Periodic force input profiles composed of two monotonic curves, as per analysis condition (b.ii) in Sect. 2.1 are directly relevant to system operation—such profiles are found, for instance, in prosthetic leg utilisation [125]. We select SEA system parameters to match the PEA system in Sect. 4.1:  $m = 1$ ,  $c = 0.8$ ,  $k = 1$ ; i.e. natural frequency,  $\omega_0 = 1$  and damping ratio  $\zeta = 0.4$ . We note that, in this system, the frequency at which a simple-harmonic input/output waveform is energy resonant is  $\omega_e$ , rather than  $\omega_0$ —these frequencies coincide in a linear PEA system, but not in a linear SEA system [20]. As per the spectral shaping process (Sect. 3.2) we seek a tuning function,  $\alpha(\omega)$ , such that the system satisfies the SEA equality conditions (Eq. 10), at least over a relevant range of  $\omega$ . We will characterise this function

### A Frequency-band resonance in an SEA system



### B Inelastic and elastic power waveforms



### C Dependency on damping

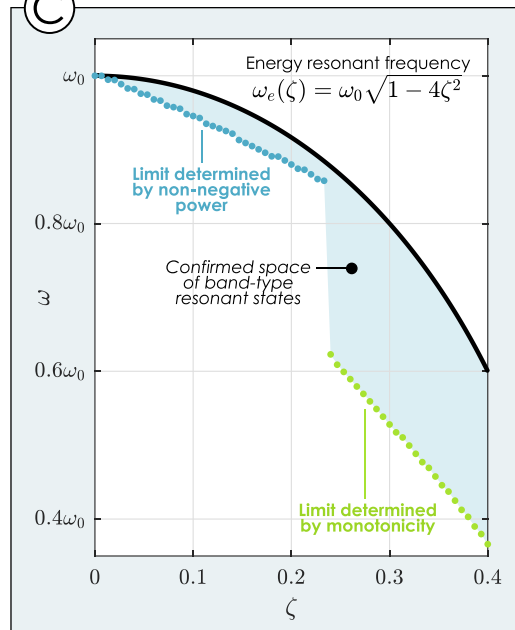


**Fig. 6** Frequency-band resonance in a linear SEA system. **A** Frequency-band resonant states in a linear SEA system, for  $\zeta = 0.4$ , computed via Algorithm 1. The SEA elastic-bound conditions (Eq. 9, Figs. 2 and 3) can be seen to be satisfied across the space of frequency-band resonant states. Scaling parameters are the compliance,  $1/k$ , and the initial simple-harmonic load amplitude, given by  $\hat{F}_0^2 = \omega_e^2 \hat{x}^2 (m^2 \omega_e^2 + c^2)$ . **B** The optimality of these states can additionally be seen in the system's power waveforms: over the space of frequency-band resonant states, the system's elastic power waveform ( $F\dot{u}$ ) is free from negative power. The scaling parameter is the initial net power  $\hat{P}_{\text{res},0} = c\hat{x}^2 \omega_e^2$ . **C** The size of the space of band-type resonant states (in decreasing frequency, and the multiharmonic waveform of Eq. 20) as a function of the SEA system damping ratio,  $\zeta$ . A complex set of factors determines the size of this space as a function of  $\zeta$ : both the energy resonance condition itself (non-negative power), and the analysis condition that  $F(t)$  varies monotonically from  $\max(F)$  to  $\min(F)$ ; and monotonically from  $\min(F)$  back to  $\max(F)$ . Outside this monotonicity condition our analysis is not formally valid, though numerically, band-type resonant states can still be computed, and still appear to be energy resonant (Fig. 7)

numerically. At a specified  $\omega$ , we formulate an algorithm for computing  $\alpha(\omega)$ —in this linear SEA system, as well as other nonlinear SEA systems. Such an algorithm can be constructed in a number of ways, but must in general contain two components: (i) a method for estimating the SEA work loop derivative  $X^{\pm'}(F=0)$  (Eq. 10), for some given value of  $\alpha$  and  $\omega$ , and thus, for estimating the error in the SEA equality condition at this  $\alpha$  and  $\omega$ ; and (ii) a method for solving for a value,  $\alpha(\omega)$ , such that this error is minimised. For the first component, our particular implementation uses the chain rule for evaluating  $X^{\pm'}$ :

$$\begin{aligned} X^{\pm'}(F(t)) &= \frac{d}{dF} X^{\pm}(F(t)) = \frac{d}{dF} x(t) \\ &= \frac{d}{dt} x(t) \bigg/ \frac{d}{dt} F(t) = \frac{\dot{x}(t)}{\dot{F}(t)}. \end{aligned} \quad (22)$$

That is, given  $\alpha$  and  $\omega$ , we begin with,  $\dot{x}(t)$  and  $\dot{F}(t)$ , functions of time, as evaluated from the waveform definition (Eq. 20) and system dynamics (Eq. 21). We can translate these functions of time to evaluations at force, and particularly, at  $F=0$ , for  $X^{\pm'}(0)$ . To do this, we must compute the critical time-values  $t^* : F(t^*) = 0$ . This can be done using numerical root-finding: preferably, through a globally convergent method, as there will typically be at least two roots of interest, associated with  $X^{+'}$  and  $X^{-'}$ , respectively. With this  $t^*$ , we can compute  $X^{\pm'}(0)$

via Eq. 22, and estimate the error in the SEA equality condition, Eq. 10:  $E(\alpha) = X^{\pm'}(0) + (F_s^{-1})'(0)$ , where  $(F_s^{-1})'(0)$  is computed from the known system elasticity. To solve then for the value of  $\alpha(\omega)$ , as per our second component, we use a root-finding method based on interpolation to compute the zeros of the error, namely  $\alpha^*$  such that  $E(\alpha^*) = 0$  over a relevant interval of the value  $\alpha(\omega)$ . Typically, there is only one zero, and we take  $\alpha(\omega) = \alpha^*$ .

This numerical method is given in Algorithm 1 below. Its results, for the linear system of Eq. 21, are illustrated in Fig. 6: the system's inelastic work loops at different frequencies, tuned according to  $\alpha(\omega)$ , and the load, displacement, and power waveforms. The tuning process ensures that these work loops represent a constant output displacement amplitude, but differing input/output displacement waveforms. As such, these work loops represent also differing force amplitudes and waveforms. These waveforms are illustrated in Fig. 6A. In the limit state,  $\omega = 0.61 \omega_0$ , the force waveform,  $F(t)$  is on the cusp of breaking the analysis monotonicity condition—that  $F(t)$  must vary monotonically from  $\max(F)$  to  $\min(F)$ ; and monotonically from  $\min(F)$  back to  $\max(F)$ . We can confirm that all these states are indeed energy resonant in two ways. *First*, we can confirm that the elastic-bound conditions (Eq. 6) are satisfied, by observing  $X^{\pm'}(F)$ . *Second*, we can observe the power requirement waveform,  $P = F\dot{u}$ , itself (Fig. 6B). In the inelastic case, in which the system's fixed elasticity is taken as absent, negative power persists in the system. In the elastic case, in which the system's fixed elasticity is present, this negative power is eliminated: these states are energy resonant. We can also use this algorithm to explore the properties of the set of band-type resonant states as a function of system damping ratio ( $\zeta$ ), as illustrated in Fig. 6C. Incrementing  $\zeta$  numerically, we can compute band-type resonant states at frequencies below  $\omega_e$ ; estimate the minimum possible frequency (with the waveform of Eq. 20); and study the factors determining this minimum. We note three interesting points. (i) The trend of energy resonant frequency,  $\omega_e$ , with damping ratio,  $\zeta$ , is strong, and leads to  $\omega_e$  substantially lower than  $\omega_0$  at high damping (e.g.  $\zeta = 0.4$ ). (ii) The size of the space of band-type resonant states does not necessarily increase in size monotonically with frequency, but may shrink (e.g. over  $0.15 < \zeta < 0.2$ ). (iii) The factor determining the

limits of the space of band-type resonant states may change with frequency. Over  $c$ ,  $0 < \zeta < 0.23$ , this space is limited by the energy resonance condition; whereas over  $c$ ,  $0.23 < \zeta < 0.4$ , the space is limited by the analysis monotonicity condition—that  $F(t)$  should vary monotonically from  $\max(F)$  to  $\min(F)$ ; and monotonically from  $\min(F)$  back to  $\max(F)$ .

Algorithm 1 is also directly applicable to nonlinear systems. Figure 7 shows an application of this algorithm to a SEA system with quadratic damping:  $D(\dot{x}, \ddot{x}) = m\ddot{x} + c\dot{x}|\dot{x}|$ , with  $c/m = 0.8$ . Quadratic damping of this form could represent, for example, a higher-fidelity model of an insect flight motor or FW-MAV [45]. In this system, frequency-band resonant states exist as low as  $\omega = 0.80 \omega_e$ : at least 20% frequency reduction with respect to the simple-harmonic energy resonant frequency (at  $\alpha = 0$ ). Note that, in both these linear and nonlinear examples, Algorithm 1 appears to continue to generate band-type resonant states even beyond the monotonicity condition: for  $F(t)$  that does *not* vary monotonically from  $\max(F)$  to  $\min(F)$ ; and/or monotonically from  $\min(F)$  back to  $\max(F)$  (Sect. 2.1). In the linear analysis (Fig. 6), although the monotonicity condition was violated for  $\omega < 0.61 \omega_e$ , the algorithm produced energy resonant states for lower values of  $\omega$  (not shown). In the nonlinear analysis (Fig. 7), examining the waveforms for  $\omega = 0.85 \omega_e$  and  $0.80 \omega_e$  indicates that they violate the monotonicity condition but are still energy resonant, as they are free from negative power.

The significance of the SEA band-type resonant states studied in this section is thus twofold. In a theoretical context, these states demonstrate the breadth of band-type resonance as a dynamical systems phenomenon. They illustrate, for instance, that band-type resonance is not simply a property of parallel-elastic (PEA) systems, but a much broader phenomenon. We can countenance the existence of band-type resonance in hybrid systems [20], and systems with multiple actuators [89]. In addition, the existence of band-type resonant states outside of the monotonicity conditions that we have applied in our analysis points to further extensions to our theoretical framework. In a practical context, these SEA band-type resonant states are directly relevant to several practical control problems: wingbeat frequency modulation in insects and FW-MAVs showing a series-elastic character [20]; efficient modulation of walking speed in series-elastic legged robots [60]; and

frequency control of atomic force microscopes [32, 33]. Our numerical method for locating band-type resonant states is particularly relevant in a practical context, as it is applicable to a wide range of systems—and could be a key component in closed-loop control strategies for energetically optimal frequency modulation in realistic, uncertain systems.

---

**Algorithm 1:** A numerical algorithm, based on interpolation, for spectral shaping in SEA systems: valid for  $\alpha(\omega)$  (Eq. 20), or other single-parameter variable waveforms. The algorithm input is a frequency,  $\omega$ , at which a candidate energy resonant state (*i.e.*, a state satisfying the SEA equality conditions, Eq. 10) is desired; its output is an estimation of the appropriate tuning function value  $\alpha(\omega)$ .

---

- 0 **Input:**  $\omega$  at which an energy resonant state is desired.
  - 1 Define basic functions  $x(t, \alpha)$ ,  $\dot{x}(t, \alpha)$ ,  $F(t, \alpha)$ , and  $\dot{F}(t, \alpha)$ , as functions of time  $t$  and tuning parameter  $\alpha$ , from waveform definition and system dynamics (Eqs. 20–21)
  - 2 Define derivative function:  $\partial x / \partial F(t, \alpha) = \dot{x}(t, \alpha) / \dot{F}(t, \alpha)$  (Eq. 22)
  - 3 Define a time-series vector  $\mathbf{t} \in [0, T]$ ,  $T = 2\pi/\omega$ , and an  $\alpha$ -vector,  $\boldsymbol{\alpha}$ , over some suitable interval of  $\alpha$ .
  - 4 Define and compute system critical compliance  $(F_s^{-1})'(F = 0)$ , from known system elasticity.
  - 5 **For**  $\alpha_i \in \boldsymbol{\alpha}$ :
  - 6 Find the values of  $t^*$  by solving  $F(t_{ij}^*, \alpha_i) = 0$ . We do this by evaluating  $\mathbf{F}_i = F(\mathbf{t}, \alpha_i)$ , constructing an interpolant  $\tilde{F}(t, \alpha_i)$  from  $\mathbf{F}_i$  and  $\boldsymbol{\alpha}$ , and evaluating  $t_{ij}^* : \tilde{F}(t_{ij}^*, \alpha_i) = 0$ .
  - 7 **Check:** that there are only two  $t_{ij}^*$  ( $j \in \{1, 2\}$ ). If not, the value of  $X_i'(0)$  is undefined and we proceed to the next  $\alpha_i$
  - 8 Evaluate the derivative  $\partial x / \partial F$  at  $t_{ij}^*$ :  $\{X_{ij}'(0)\} = \{\partial x / \partial F(t_{ij}^*, \alpha_i)\}$ ,  $j \in \{1, 2\}$ . This step uses the result of line 2, according to Eq. 22.
  - 9 **Check:** that  $X_{i,1}'(0) = X_{i,2}'(0)$ , and if so, define this common value as  $X_i'(0)$ . If not, return  $X_i'(0)$  as undefined.
  - 10 **End** loop, return series  $X_i'(0)$  as vector,  $\mathbf{X}'(0)$ .
  - 11 Compute error  $\mathbf{E} = \mathbf{X}'(0) + (F_s^{-1})'(0)$ .
  - 12 Construct an interpolant  $\tilde{E}(\alpha)$ , from  $\mathbf{E}$  and  $\boldsymbol{\alpha}$ , and evaluate all  $\alpha_k^* : \tilde{E}(\alpha_k^*) = 0$ .
  - 13 **Output:** all  $\alpha_k^*$  are tuning parameters such that the waveform  $x(t, \alpha)$  satisfies the SEA equality conditions at the specified  $\omega$
-

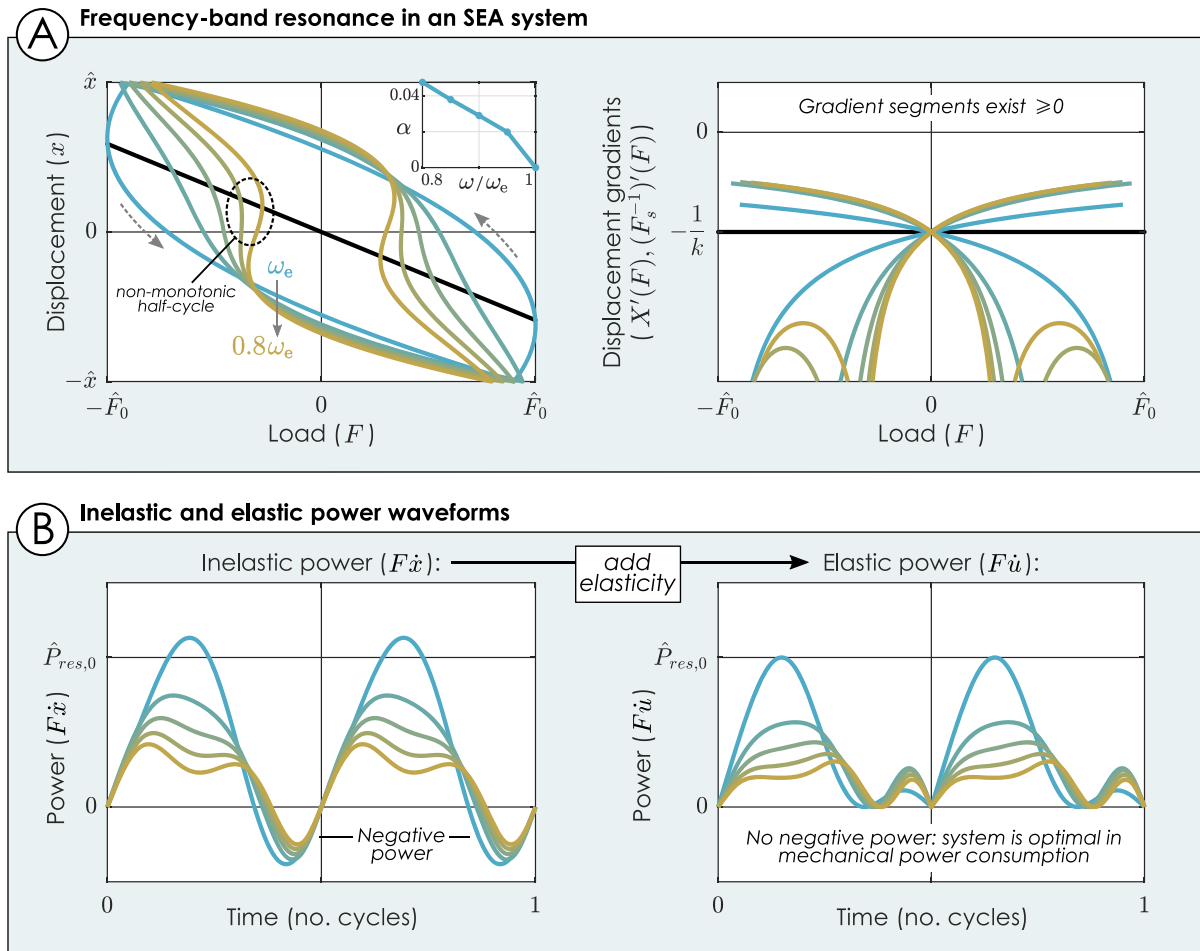


**Fig. 7** Frequency-band resonance in a nonlinear SEA system. **A** Frequency-band resonant states in a quadratically damped nonlinear SEA system, computed via Algorithm 1. Note that these states do not satisfy the monotonicity condition in  $F(t)$  for  $\omega = 0.85 \omega_e$  and  $0.80 \omega_e$ , as indicated. Scaling parameters are the compliance,  $1/k$ , and the initial simple-harmonic load amplitude,  $\hat{F}_0$ . **B** The optimality of these states, even those

which do not satisfy the monotonicity condition in  $F(t)$ , can be seen in the system's power waveforms. Over the space of frequency-band resonant states, the system's elastic power waveform ( $F\dot{u}$ ) is free from negative power. The scaling parameter is the initial net power  $\hat{P}_{res,0}$

## 5 Discussion

### 5.1 Implications for biolocomotion systems

The principles of frequency-band and offset-band resonance have significant practical implications for biolocomotion systems. These principles demonstrate, in a fundamental way, that frequency and offset modulation, as well as other forms of waveform modulation, are available at a state of continual energetic optimality—a state of energy resonance at fixed structural elasticity. In insects, for instance, the

phenomenon of frequency-band resonance indicates that insects are able to achieve resonant oscillations of the wing-motor system not only at a single frequency, but over a range of frequencies, providing the insect can tolerate slight alterations in the wing-stroke kinematics and/or muscular load waveform as a necessary cost. A range of insect species are observed to use wingbeat frequency modulation for a range of purposes: for aerodynamic force control [44, 77–79]; for acoustic courtship interactions [90, 118]; and for temperature regulation [80, 119]. This modulation has conventionally been explained as either the result of



possible real-time resonant frequency control mechanisms within the thorax [44, 46, 86–89], or in terms of the trade-off involved in deviating from resonance [44]. In contrast, our results (Sect. 4.1) suggest that wingbeat frequency modulation need not incur significant energetic costs—wingbeat frequency modulation via frequency-band resonance can be achieved without leaving a state of optimality in mechanical power consumption. By the same token, offset-band resonance provides explanations for mechanisms of body pitch control in insects such as fruit flies. This form of pitch-axis control involves modulating the asymmetry of the resonant state: independent modulation of the wing stroke angle extrema ( $\max x$  and  $\min x$ , as per Sect. 4.2). Offset-band resonance can ensure that this control is achieved at a continual state of energy resonance. Indeed, ensuring the energetic optimality of this control is made more urgent by the fact that the fruit fly free-flight pitch dynamics are unstable [83, 123], necessitating that pitch-axis control should be continually active.

Band-type resonance also elucidates a more fundamental effect in biolocomotion, and in flapping-wing flight: it illustrates how different input/output waveforms have different energy resonant frequencies. Insect wing stroke waveforms are typically not simple-harmonic, but instead can show a triangle-wave character [95]. As illustrated in Sect. 4.1, triangle-type waves can have significantly lower energy resonant frequencies than simple-harmonic waveforms—and this difference is of sufficient magnitude to explain resonant frequency discrepancies observed in the literature [42]. Together, band-type resonance principles elucidate several aspects of insect flight behaviour. They apply also to the design of FW-MAVs, and other biomimetic systems: for instance, micro-swimmers driven by external acoustic or magnetic fields [57, 58], and prosthetic and robotic leg structures [61, 62]. There is significant scope for more specific studies of the role of band-type resonance in biolocomotion, as well as for further theoretical development in this area—in particular, further study of the more complex dynamical systems (e.g. hybrid PEA-SEA [20], and multiple-input [89] systems) that arise in many biological locomotive structures.

## 5.2 Optimality in composite cost metrics

Band-type resonant states are energy resonant: they show optimal mechanical power consumption with respect to elasticity. In a system with some fixed elasticity, if a particular kinematic output is band-type resonant ( $x_i \in \mathcal{X}$ , Sect. 3.1), then it is not possible to choose a different elasticity such that this kinematic output can be generated at a lower overall mechanical power consumption. However, in band-type resonant states it is not only the overall mechanical power consumption which is optimal (with respect to elasticity). The principles of invariance (Sect. 2.3) imply that these band-type resonant states are also optimal in any invariant metrics associated with the system. For instance, in PEA systems, the absolute force metric ( $\bar{P}_{|F|}$ , Eq. 5) is invariant across the space of energy resonant elasticities, if the kinematic output waveform satisfies the symmetry condition  $x(t) = x(T - t), \forall t$  (Sect. 2.3). Therefore, if the PEA band-type resonant states satisfy this symmetry condition (e.g. as in the frequency-band resonance studied in Sect. 4.1) then these states are optimal also in  $\bar{P}_{|F|}$ . It is impossible to choose a different elasticity such that  $\bar{P}_{|F|}$  is further minimised. In SEA systems, any functionals of solely  $F(t)$ , including the force-squared metric ( $\bar{P}_{F^2}$ ), and peak load ( $\hat{F}$ ) are invariant across the entire space of possible elasticities. Any SEA band-type resonant state is optimal (with respect to elasticity) in any of these functionals of  $F(t)$ : it is impossible to choose a different elasticity such that, for example, the peak load is further minimised.

In this way, the invariance principles of Sect. 2.3 lead to powerful optimality principles for band-type resonant states—defining a suite of composite cost metrics which are guaranteed to be optimal with respect to elasticity, at any band-type resonant output ( $x_i \in \mathcal{X}$ ). These optimality principles have particular practical importance in the context of choices between different frequency and offset modulation strategies. As noted in Sect. 5.1, in insects, the action of sets of auxiliary muscles has been proposed as a mechanism for real-time tuning thoracic elasticity—potentially allowing wingbeat frequency modulation while maintaining a conventional simple-harmonic resonant state [44, 46, 86–89]. Real-time elasticity tuning strategies come at additional cost in energy, actuator complexity, and control architecture, but can lead to more optimal

modulated states than band-type resonant control. At any modulated state, one can (hypothetically) choose a tuned elasticity to minimise any desired cost metric. In this context, the composite-metric optimality principles for band-type resonant states help elucidate which metrics real-time elasticity tuning can further minimise, and which metrics it cannot. Over the space of band-type resonant states, invariant metrics (e.g. peak force in SEA systems) cannot be minimised further by real-time elasticity tuning—hence, there is little motivation for such tuning. Metrics that are not invariant (e.g. peak force in PEA systems), on the other hand, can be minimised further—it is thus possible that the implementation costs of real-time elasticity tuning could be outweighed by this additional metric minimisation.

The topic of composite-metric optimality has significant practical implications for biolocomotion. Consider two versions of a biolocomotive system (e.g. a flapping-wing system): one driven by biological muscles, and one driven by an electromechanical actuator. The isometric power consumption of these two actuators—i.e. the power consumption when the actuator is exerting a force, but not moving—is different. In the biological muscle, the isometric power consumption can be measured by the absolute force metric,  $\bar{P}_{|F|}$ , among other metrics [100, 106–108]. In the electromechanical actuator, the isometric power consumption is measured by the resistive losses; the force-squared metric,  $\bar{P}_{F^2}$  [113, 114]. If this biolocomotive system is driven in a PEA architecture, then it can benefit from optimality in  $\bar{P}_{|F|}$  (an invariant metric), but not in  $\bar{P}_{F^2}$  (a non-invariant metric). We assume, implicitly, that these isometric power losses will be also present when the system is not static. If this is the case, the biological system will be energetically optimal in isometric power consumption, but the electromechanical system will not. This is a crucial distinction: if, for instance, wingbeat frequency modulation strategies employed by insects take advantage of invariance-based optimality in muscular power consumption, then these same modulation strategies translated to electromechanically driven FW-MAVs may no longer be optimal. In this way, subtle differences in the behaviour of biological and electromechanical actuators could lead to significant degradations in optimality when biological design principles are translated

directly to biomimetic robots—illustrating the importance of considering these invariance principles in biolocomotive systems design and control.

### 5.3 Band-type resonance as optimal control

The band-type resonant control proposed in Sect. 5.1 appears to have significant connections to other areas of control theory. Firstly, while we have utilised an inverse-problem approach to study the theoretical properties of band-type resonant states in 1DOF nonlinear systems, this approach motivates forward-problem approaches for generating band-type resonant states in a closed-loop control context. For instance, a closed-loop control strategy for generating band-type resonant states could involve initially generating a unidirectional force ( $F$ ), monitoring the actuation point velocity ( $\dot{x}$ ), and switching actuator force direction in order to maintain  $F\dot{x} > 0$  (energy resonance). There is significant scope for further development of such control strategies. Secondly, we conjecture that there is a link between band-type resonance and optimal control theory. Band-type resonant states show certain optimality properties with respect to mechanical power: a cost metric sometimes expressible as a quadratic form. That is, if we represent a linear PEA or SEA system as the first-order controlled system:

$$\dot{\mathbf{x}} = \mathbf{A}\mathbf{x} + \mathbf{B}\mathbf{u}, \quad (23)$$

where we have  $\mathbf{u} = F$  and  $\mathbf{x} = [x, \dot{x}]^T$ , then cost functionals based on net and absolute mechanical power,  $J_{(a)}$  and  $J_{(b)}$ , respectively, can be defined as:

$$\begin{aligned} J_{(a)} &= \int_{t_0}^{t_h} \mathbf{u}^T \mathbf{Q} \mathbf{x} \, dt = \int_{t_0}^{t_h} F \dot{x} \, dt, \\ J_{(b)} &= \int_{t_0}^{t_h} |\mathbf{u}^T \mathbf{Q} \mathbf{x}| \, dt = \int_{t_0}^{t_h} \mathbf{u}^T [0, \text{sgn}(\mathbf{u}^T \mathbf{Q} \mathbf{x})] \mathbf{x} \, dt = \int_{t_0}^{t_h} |F \dot{x}| \, dt, \end{aligned} \quad (24)$$

where  $[t_0, t_h]$  is the control interval and the quadratic cost matrix is  $\mathbf{Q} = [0, 1]$ . Band-type resonant states necessarily ensure that  $J_{(b)}/J_{(a)} = 1$ , and the problem of locating these states can be seen as an optimal control problem to maximise  $J_{(b)}/J_{(a)}$ . In our analysis, we typically look for outputs,  $x(t)$ , that ensure energy resonant; whereas in an optimal control context, one

would look for inputs,  $F(t)$ ; but the two approaches are closely related. For instance, consider the problem of finding any periodic  $F(t)$  such that  $J_{(b)}/J_{(a)}$  takes its global maximum value ( $J_{(b)}/J_{(a)} = 1$ ). The set of solutions to this problem are contained within the system's set of band-type resonant states: they are the forcing functions,  $F_i(t)$ , encoded within  $\mathcal{S} = \{\{x_i(t), u_i(t), F_i(t)\}\}_i$  (Sect. 3.1). Or, consider the more specific problem of finding a periodic  $F(t)$ , with specified periodic frequency  $\omega$ , such that  $J_{(b)}/J_{(a)} = 1$ . The set of solutions to this problem, if any exist, can be found within the system's set of frequency-band resonant states at  $\omega$ —particular examples of which are given in Sects. 5.1 and 5.3, for linear PEA and SEA systems.

In our analysis, to define, for example, the frequency-band resonant states in Sects. 5.1 and 5.3, we assumed that the exact dynamics of the system were known. This contrasts with a more realistic control-system context, in which disturbances and unmodelled dynamics are likely to be present. To address the problem of finding band-type resonant states in realistic, uncertain systems, techniques from optimal control may be applicable. In particular, we observe that band-type resonant states resemble the sliding manifolds used in sliding-mode control [126, 127]. Sliding-mode control involves the use of discontinuous control laws to constrain a system to a favourable state-space manifold. An analogy is of a marble rolling along a narrow crack [128]: the crack walls (discontinuous control laws) constrain the system (the marble) to the sliding manifold (the crack). Given that an individual band-type resonant state can be represented as a steady-state phase portrait, i.e. a state-space manifold, we propose that the techniques of sliding-mode control design may be applicable to the design of controllers to constrain the system to the band-type resonant state. This is an interesting topic for future research—with relevance both for the design of controlled biomimetic propulsion systems, and the interpretation of control strategies used by biological organisms.

## 6 Conclusions

In this work, we have characterised the phenomenon of band-type resonance: a novel form of non-discrete

resonant state in linear and nonlinear forced oscillators. The phenomenon of band-type resonance has significance across theoretical and applied dynamics. On a theoretical level, band-type resonance is counterpoint to common assumptions about resonance, and energetic optimality, in forced oscillators. As we demonstrate, in both linear and nonlinear systems, the state of energetic optimality is not tied to a single frequency—e.g. the linear resonant frequency—but can exist in a band of frequencies. Nor is the state of energetic optimality tied to a particular, for example, symmetric, kinematic waveform, but can be available in a band of offset, asymmetry-modulated waveforms. Even the simple result that energetically optimal frequency modulation is available in linear PEA and SEA systems (Sects. 4.1 and 5.2) is a counterpoint to the common supposition that deviation from the linear resonant frequency necessarily involves a loss of efficiency. On a practical level, band-type resonance provides avenues for radically novel forms of resonant state control in a wide range of forced oscillators—including in biolocomotion systems, which we have considered in detail. Band-type resonance enables forms of optimal frequency (thrust/lift) and offset (steering) control in flapping-wing propulsion systems that have not previously been reported. We demonstrate how these forms of optimal control can be generated via an advanced excitation strategy: small modifications to the system drive waveforms can be utilised to generate targeted resonant modulations in frequency or output symmetry. Analytical and numerical methods for carrying out this process are developed and demonstrated. Band-type resonance also provides practical alternative explanations for a range of counterintuitive control behaviours observed in insects, including in-flight wingbeat frequency and offset modulation.

Our characterisation of band-type resonance also raises a range of further practical and theoretical open questions: regarding the relationship of band-type resonance to problems and techniques in optimal control, such as sliding-mode control; regarding the exact properties of the space of band-type resonance states in particular systems; and regarding the nature of phenomena akin to band-type resonance in systems beyond the scope of our current analysis—in multi-degree-of-freedom systems; time-varying systems, and systems undergoing non-periodic responses. Future research to resolve these open questions has

the potential to lead to new practical approaches for designing and locating band-type resonance states—and thereby, new control principles for many different forms of forced oscillator. Band-type resonance has implications not only for biological and bio-inspired locomotion systems but for a constellation of forced oscillator systems across physics, engineering, and biology.

**Acknowledgements** This work was supported by the Israel Science Foundation Grant No. 1851/17 and by the Israel Ministry of Science and Technology Grant No. 3-17400.

**Data availability** No datasets were generated or utilised in this study.

**Declarations**

**Conflict of interest** The authors declare that they have no conflict of interest.

## Appendix

### A.1 Closed-form expressions for PEA and SEA work loops

In Sect. 2.1, we defined general work-loop profiles:  $G^\pm(x)$  and  $F^\pm(x)$  for PEA systems; and  $X^\pm(F)$  and  $U^\pm(F)$  for SEA systems. These constructs can be defined analytically for a range of different systems. For a linear PEA system, with  $D(\dot{x}, \ddot{x}) = m\ddot{x} + c\dot{x}$ ,  $F_s(x) = kx$ , and undergoing simple-harmonic oscillation according to  $x(t) = \hat{x}\cos(\omega t)$ , we have [25]:

$$\begin{aligned} G^\pm(x) &= -m\omega^2 x \pm c\omega\sqrt{\hat{x}^2 - x^2}, \\ F^\pm(x) &= kx - m\omega^2 x \pm c\omega\sqrt{\hat{x}^2 - x^2}. \end{aligned} \quad (\text{A.1.1})$$

And for a quadratically damped PEA system, with  $D(\dot{x}, \ddot{x}) = m\ddot{x} + \text{sgn}(\dot{x})c\dot{x}^2$ , undergoing the same simple-harmonic motion, we have [25]:

$$\begin{aligned} G^\pm(x) &= -m\omega^2 x \pm c\omega^2(x^2 - \hat{x}^2), \\ F^\pm(x) &= kx - m\omega^2 x \pm c\omega^2(x^2 - \hat{x}^2). \end{aligned} \quad (\text{A.1.2})$$

These functions are defined for  $x \in [-\hat{x}, \hat{x}]$ . For a linear SEA system, with  $D(\dot{x}, \ddot{x}) = m\ddot{x} + c\dot{x}$ ,  $F_s(x) = kx$ , and undergoing simple-harmonic

oscillation according to  $x(t) = \hat{x}\cos(\omega t)$ , the construction is more complex. For  $X^\pm(F)$  and  $U^\pm(F)$  we have:

$$\begin{aligned} X^\pm(F) &= \frac{1}{m^2\omega^2 + c^2} \left( -mF \pm \frac{c}{\omega} \sqrt{\hat{x}^2\omega^2(m^2\omega^2 + c^2) - F^2} \right), \\ U^\pm(F) &= \frac{F}{k} + \frac{1}{m^2\omega^2 + c^2} \left( -mF \pm \frac{c}{\omega} \sqrt{\hat{x}^2\omega^2(m^2\omega^2 + c^2) - F^2} \right), \end{aligned} \quad (\text{A.1.3})$$

where these functions are defined over the force range  $F \in [-\hat{F}, \hat{F}]$ , with  $\hat{F} = \omega\hat{x}\sqrt{m^2\omega^2 + c^2}$ .

To compute the elastic-bound conditions, Eq. 6, one further profile is required: the derivatives  $X'^\pm(F)$ . These derivatives are given by:

$$X'^\pm(F) = \frac{1}{m^2\omega^2 + c^2} \left( -m \mp \frac{cF}{\omega\sqrt{\hat{x}^2\omega^2(m^2\omega^2 + c^2) - F^2}} \right). \quad (\text{A.1.4})$$

This completes the definition of work-loop profiles for these example systems.

### A.2 Generalised triangle-wave function

To analyse frequency-band resonance in Sect. 4.1, we utilised a generalised triangle-like wave, allowing waveform alteration with associated frequency and offset modulation. This waveform was described via a freeplay-nonlinear time-invariant ODE. The time-domain solution to this ODE is:

$$\begin{aligned} \ddot{x}(t) &= \begin{cases} -A(\delta) \frac{\hat{x}}{T^2} \cos\left(\frac{\pi t}{2\delta T}\right) & 0 \leq t \leq \delta T \\ A(\delta) \frac{\hat{x}}{T^2} \cos\left(\frac{\pi\left(t - \frac{1}{2}T\right)}{2\delta T}\right) & \left(\frac{1}{2} - \delta\right)T \leq t \leq \left(\frac{1}{2} + \delta\right)T \\ -A(\delta) \frac{\hat{x}}{T^2} \cos\left(\frac{\pi(t - T)}{2\delta T}\right) & T(1 - \delta) \leq t \leq T \\ 0 & \text{o.w.} \end{cases} \\ A(\delta) &= \frac{2\pi^2}{(8 - 4\pi)\delta^2 + \pi\delta}, \quad \delta = \delta(R) = \frac{1}{4} \frac{\pi(1 - R)}{(2 - \pi)R + \pi}, \end{aligned} \quad (\text{A.2.1})$$

with  $\dot{x}(t)$  and  $x(t)$  as:

$$\dot{x}(t) = \int_0^t \ddot{x}(\tau) d\tau, \quad x(t) = \int_0^t \dot{x}(\tau) d\tau + \hat{x}. \quad (\text{A.2.2})$$

The parameter  $\delta$  is a time-domain analogue of  $R$ , representing the time window over which the sinusoid velocity-reversal component acts, as per the piecewise component limits in Eq. A.2.1; and  $T$  is the waveform period,  $T = 2\pi/\omega$ . Analytical formulations of  $x(t)$ , via Eq. A.2.2, are available, but these formulations are not required for frequency-band acceleration-matching, and so we use numerical integration for convenience.

## References

1. Killingbeck, J.P.: Mathematical Techniques and Physical Applications. Elsevier, Saint Louis (2014)
2. Goldstein, H., Poole, C.P., Safko, J.L.: Classical Mechanics. Addison Wesley, Munich (2008)
3. Thomsen, J.J.: Vibrations and Stability: Advanced Theory, Analysis, and Tools. Springer, Berlin (2021)
4. Ibrahim, R.A.: Oscillons, walking droplets, and skipping stones (an overview). *Nonlinear Dyn.* **104**, 1829–1888 (2021). <https://doi.org/10.1007/s11071-021-06442-y>
5. Solomon, T.H., Mezić, I.: Uniform resonant chaotic mixing in fluid flows. *Nature* **425**, 376–380 (2003). <https://doi.org/10.1038/nature01993>
6. Inagaki, M., Murata, O., Kondoh, T., Abe, K.: Numerical prediction of fluid-resonant oscillation at low Mach number. *AIAA J.* **40**, 1823–1829 (2002). <https://doi.org/10.2514/2.1859>
7. Akram, M.J., Saif, F.: Complex dynamics of nano-mechanical membrane in cavity optomechanics. *Nonlinear Dyn.* **83**, 963–970 (2016). <https://doi.org/10.1007/s11071-015-2380-y>
8. Chen, W., Roelli, P., Hu, H., Verlekar, S., Amirtharaj, S.P., Barreda, A.I., Kippenberg, T.J., Kovylina, M., Verhagen, E., Martínez, A., Galland, C.: Continuous-wave frequency upconversion with a molecular optomechanical nanocavity. *Science* **374**, 1264–1267 (2021). <https://doi.org/10.1126/science.abk3106>
9. Wang, F., Dukovic, G., Brus, L.E., Heinz, T.F.: The optical resonances in carbon nanotubes arise from excitons. *Science* **308**, 838–841 (2005). <https://doi.org/10.1126/science.1110265>
10. Bird, J.O.: Electrical Circuit Theory and Technology. Newnes, Oxford (2007)
11. Jothimurugan, R., Thamilmaran, K., Rajasekar, S., Sanjuán, M.A.F.: Multiple resonance and anti-resonance in coupled Duffing oscillators. *Nonlinear Dyn.* **83**, 1803–1814 (2016). <https://doi.org/10.1007/s11071-015-2447-9>
12. Zhang, B., Shu, X.: Fractional-Order Electrical Circuit Theory. Springer, Cham (2022)
13. Karev, A., Hagedorn, P.: Asynchronous parametric excitation: validation of theoretical results by electronic circuit simulation. *Nonlinear Dyn.* **102**, 555–565 (2020). <https://doi.org/10.1007/s11071-020-05870-6>
14. Shuvaev, A., Muravev, V.M., Gusikhin, P.A., Gospodarič, J., Pimenov, A., Kukushkin, I.V.: Discovery of two-dimensional electromagnetic plasma waves. *Phys. Rev. Lett.* **126**, 136801 (2021). <https://doi.org/10.1103/PhysRevLett.126.136801>
15. Qi, Z., Chen, Q., Wang, M., Li, B.: New mixed solutions generated by velocity resonance in the (2+1)-dimensional Sawada–Kotera equation. *Nonlinear Dyn.* **108**, 1617–1626 (2022). <https://doi.org/10.1007/s11071-022-07248-2>
16. Rajasekar, S., Sanjuán, M.A.F.: Nonlinear Resonances. Springer, Cham (2016)
17. Kartashova, E.: Nonlinear Resonance Analysis: Theory, Computation, Applications. Cambridge University Press, Cambridge (2011)
18. Awrejcewicz, J. (ed.): Resonance. InTech, London (2017)
19. Gammaitoni, L., Hänggi, P., Jung, P., Marchesoni, F.: Stochastic resonance. *Rev. Mod. Phys.* **70**, 223–287 (1998). <https://doi.org/10.1103/RevModPhys.70.223>
20. Pons, A., Beatus, T.: Distinct forms of resonant optimality within insect indirect flight motors. *J. R. Soc. Interface* (2022). <https://doi.org/10.1098/rsif.2022.0080>
21. Ma, T., Zhang, H.: Reaping the potentials of nonlinear energy harvesting with tunable damping and modulation of the forcing functions. *Appl. Phys. Lett.* **104**, 214104 (2014). <https://doi.org/10.1063/1.4879846>
22. Zhang, H., Ma, T.: Roles of the excitation in harvesting energy from vibrations. *PLoS ONE* **10**, e0141299 (2015). <https://doi.org/10.1371/journal.pone.0141299>
23. Zhang, H., Ma, T., Xu, N.S.: New insights into vibration-based energy harvesting. In: Proceedings of the SPIE 9435, Sensors and Smart Structures Technologies for Civil, Mechanical, and Aerospace Systems, pp. 943504, SPIE, San Diego (2015)
24. Zhang, H., Corr, L.R., Ma, T.: Issues in vibration energy harvesting. *J. Sound Vib.* **421**, 79–90 (2018). <https://doi.org/10.1016/j.jsv.2018.01.057>
25. Pons, A., Beatus, T.: Elastic-bound conditions for energetically optimal elasticity and their implications for biomimetic propulsion systems. *Nonlinear Dyn.* **108**, 2045–2074 (2022). <https://doi.org/10.1007/s11071-022-07325-6>
26. Vakakis, A.F., Gendelman, O.V., Bergman, L.A., Mojahe, A., Gzal, M.: Nonlinear targeted energy transfer: state of the art and new perspectives. *Nonlinear Dyn.* **108**, 711–741 (2022). <https://doi.org/10.1007/s11071-022-07216-w>
27. Brand, O., Dufour, I., Heinrich, S.M., Josse, F. (eds.): Resonant MEMS: Fundamentals, Implementation and Application. Wiley, Weinheim (2015)
28. Ilyas, S., Alfossail, F.K., Bellaredj, M.L.F., Younis, M.I.: On the response of MEMS resonators under generic electrostatic loadings: experiments and applications. *Nonlinear Dyn.* **95**, 2263–2274 (2019). <https://doi.org/10.1007/s11071-018-4690-3>
29. Indeitsev, D.A., Belyaev, Y.V., Lukin, A.V., Popov, I.A.: Nonlinear dynamics of MEMS resonator in PLL-AGC self-oscillation loop. *Nonlinear Dyn.* **104**, 3187–3204 (2021). <https://doi.org/10.1007/s11071-021-06586-x>
30. Ruzziconi, L., Jaber, N., Kosuru, L., Bellaredj, M.L., Younis, M.I.: Internal resonance in the higher-order modes of a MEMS beam: experiments and global analysis.



- Nonlinear Dyn. **103**, 2197–2226 (2021). <https://doi.org/10.1007/s11071-021-06273-x>
31. Guillon, S., Saya, D., Mazenq, L., Perisanu, S., Vincent, P., Lazarus, A., Thomas, O., Nicu, L.: Effect of non-ideal clamping shape on the resonance frequencies of silicon nanocantilevers. *Nanotechnology* **22**, 245501 (2011). <https://doi.org/10.1088/0957-4484/22/24/245501>
  32. Gutschmidt, S., Gottlieb, O.: Nonlinear dynamic behavior of a microbeam array subject to parametric actuation at low, medium and large DC-voltages. *Nonlinear Dyn.* **67**, 1–36 (2012). <https://doi.org/10.1007/s11071-010-9888-y>
  33. Hornstein, S., Gottlieb, O.: Nonlinear dynamics, stability and control of the scan process in noncontacting atomic force microscopy. *Nonlinear Dyn.* **54**, 93–122 (2008). <https://doi.org/10.1007/s11071-008-9335-5>
  34. Chandrashekar, A., Belardinelli, P., Staufer, U., Alijani, F.: Robustness of attractors in tapping mode atomic force microscopy. *Nonlinear Dyn.* **97**, 1137–1158 (2019). <https://doi.org/10.1007/s11071-019-05037-y>
  35. Rega, G., Settimi, V.: Bifurcation, response scenarios and dynamic integrity in a single-mode model of noncontact atomic force microscopy. *Nonlinear Dyn.* **73**, 101–123 (2013). <https://doi.org/10.1007/s11071-013-0771-5>
  36. Berardengo, M., Manzoni, S., Thomas, O., Vanali, M.: Piezoelectric resonant shunt enhancement by negative capacitances: optimisation, performance and resonance cancellation. *J. Intell. Mater. Syst. Struct.* **29**, 2581–2606 (2018). <https://doi.org/10.1177/1045389X18770874>
  37. Shami, Z.A., Giraud-Audine, C., Thomas, O.: A nonlinear piezoelectric shunt absorber with 2:1 internal resonance: experimental proof of concept. *Smart Mater. Struct.* **31**, 035006 (2022). <https://doi.org/10.1088/1361-665X/ac4ab5>
  38. Shami, Z.A., Giraud-Audine, C., Thomas, O.: A nonlinear piezoelectric shunt absorber with a 2:1 internal resonance: theory. *Mech. Syst. Signal Process.* **170**, 108768 (2022). <https://doi.org/10.1016/j.ymssp.2021.108768>
  39. Xia, Y., Ruzzene, M., Erturk, A.: Bistable attachments for wideband nonlinear vibration attenuation in a metamaterial beam. *Nonlinear Dyn.* **102**, 1285–1296 (2020). <https://doi.org/10.1007/s11071-020-06008-4>
  40. Cveticanin, L., Zukovic, M., Cveticanin, D.: Influence of nonlinear subunits on the resonance frequency band gaps of acoustic metamaterial. *Nonlinear Dyn.* **93**, 1341–1351 (2018). <https://doi.org/10.1007/s11071-018-4263-5>
  41. Hrncir, M., Gravel, A.-I., Schorkopf, D.L.P., Schmidt, V.M., Zucchi, R., Barth, F.G.: Thoracic vibrations in stingless bees (*Melipona seminigra*): resonances of the thorax influence vibrations associated with flight but not those associated with sound production. *J. Exp. Biol.* **211**, 678–685 (2008). <https://doi.org/10.1242/jeb.013920>
  42. Jankauski, M.A.: Measuring the frequency response of the honeybee thorax. *Bioinspir. Biomim.* **15**, 046002 (2020). <https://doi.org/10.1088/1748-3190/ab835b>
  43. Gau, J., Gravish, N., Sponberg, S.: Indirect actuation reduces flight power requirements in *Manduca sexta* via elastic energy exchange. *J. R. Soc. Interface* **16**, 20190543 (2019). <https://doi.org/10.1098/rsif.2019.0543>
  44. Gau, J., Gemilere, R., Lynch, J., Gravish, N., Sponberg, S.: Rapid frequency modulation in a resonant system: aerial perturbation recovery in hawkmoths. *Proc. R. Soc. B Biol. Sci.* **288**, 20210352 (2021). <https://doi.org/10.1098/rspb.2021.0352>
  45. Lynch, J., Gau, J., Sponberg, S., Gravish, N.: Dimensional analysis of spring-wing systems reveals performance metrics for resonant flapping-wing flight. *J. R. Soc. Interface* **18**, 20200888 (2021). <https://doi.org/10.1098/rsif.2020.0888>
  46. Lehmann, F.O., Dickinson, M.H.: The control of wing kinematics and flight forces in fruit flies (*Drosophila* spp.). *J. Exp. Biol.* **201**, 385 (1998). <https://doi.org/10.1242/jeb.201.3.385>
  47. Deora, T., Singh, A.K., Sane, S.P.: Biomechanical basis of wing and haltere coordination in flies. *Proc. Natl. Acad. Sci.* **112**, 1481–1486 (2015). <https://doi.org/10.1073/pnas.1412279112>
  48. Hoover, A., Miller, L.: A numerical study of the benefits of driving jellyfish bells at their natural frequency. *J. Theor. Biol.* **374**, 13–25 (2015). <https://doi.org/10.1016/j.jtbi.2015.03.016>
  49. Hoover, A.P., Porras, A.J., Miller, L.A.: Pump or coast: the role of resonance and passive energy recapture in medusan swimming performance. *J. Fluid Mech.* **863**, 1031–1061 (2019). <https://doi.org/10.1017/jfm.2018.1007>
  50. Hoover, A.P., Xu, N.W., Gemmell, B.J., Colin, S.P., Costello, J.H., Dabiri, J.O., Miller, L.A.: Neuromechanical wave resonance in jellyfish swimming. *Proc. Natl. Acad. Sci.* **118**, e2020025118 (2021). <https://doi.org/10.1073/pnas.2020025118>
  51. Bhalla, A.P.S., Griffith, B.E., Patankar, N.A.: A forced damped oscillation framework for undulatory swimming provides new insights into how propulsion arises in active and passive swimming. *PLOS Comput. Biol.* **9**, e1003097 (2013). <https://doi.org/10.1371/journal.pcbi.1003097>
  52. Kohannim, S., Iwasaki, T.: Analytical insights into optimality and resonance in fish swimming. *J. R. Soc. Interface* **11**, 20131073 (2014). <https://doi.org/10.1098/rsif.2013.1073>
  53. Tytell, E.D., Hsu, C.-Y., Fauci, L.J.: The role of mechanical resonance in the neural control of swimming in fishes. *Zoology* **117**, 48–56 (2014). <https://doi.org/10.1016/j.zool.2013.10.011>
  54. Ahlborn, B.K., Blake, R.W.: Walking and running at resonance. *Zoology* **105**, 165–174 (2002). <https://doi.org/10.1078/0944-2006-00057>
  55. Bujard, T., Giorgio-Serchi, F., Weymouth, G.D.: A resonant squid-inspired robot unlocks biological propulsive efficiency. *Sci. Robot.* **6**, eabd2971 (2021). <https://doi.org/10.1126/scirobotics.abd2971>
  56. Zhang, C., Rossi, C.: A review of compliant transmission mechanisms for bio-inspired flapping-wing micro air vehicles. *Bioinspir. Biomim.* **12**, 025005 (2017). <https://doi.org/10.1088/1748-3190/aa58d3>
  57. Kaynak, M., Ozcelik, A., Nourhani, A., Lammert, P.E., Crespi, V.H., Huang, T.J.: Acoustic actuation of bio-inspired microswimmers. *Lab Chip* **17**, 395–400 (2017). <https://doi.org/10.1039/C6LC01272H>
  58. Liu, J., Ruan, H.: Modeling of an acoustically actuated artificial micro-swimmer. *Bioinspir. Biomim.* **15**, 036002 (2020). <https://doi.org/10.1088/1748-3190/ab6a61>
  59. Ramanarivo, S., Godoy-Diana, R., Thiria, B.: Passive elastic mechanism to mimic fish-muscle action in

- anguilliform swimming. *J. R. Soc. Interface* **10**, 20130667 (2013). <https://doi.org/10.1098/rsif.2013.0667>
60. Collins, S., Ruina, A., Tedrake, R., Wisse, M.: Efficient bipedal robots based on passive-dynamic walkers. *Science* **307**, 1082–1085 (2005). <https://doi.org/10.1126/science.1107799>
  61. Haldane, D.W., Plecnik, M.M., Yim, J.K., Fearing, R.S.: Robotic vertical jumping agility via series-elastic power modulation. *Sci. Robot.* **1**, eaag2048 (2016). <https://doi.org/10.1126/scirobotics.aag2048>
  62. Bolivar Nieto, E.A., Rezazadeh, S., Gregg, R.D.: minimizing energy consumption and peak power of series elastic actuators: a convex optimization framework for elastic element design. *IEEE ASME Trans. Mechatron.* **24**, 1334–1345 (2019). <https://doi.org/10.1109/TMECH.2019.2906887>
  63. Taha, H.E., Nayfeh, A.H., Hajj, M.R.: Saturation-based actuation for flapping MAVs in hovering and forward flight. *Nonlinear Dyn.* **73**, 1125–1138 (2013). <https://doi.org/10.1007/s11071-013-0857-0>
  64. Bauer, F., Römer, U., Fidlín, A., Seemann, W.: Optimization of energy efficiency of walking bipedal robots by use of elastic couplings in the form of mechanical springs. *Nonlinear Dyn.* **83**, 1275–1301 (2016). <https://doi.org/10.1007/s11071-015-2402-9>
  65. Bauer, F., Fidlín, A., Seemann, W.: Energy efficient bipedal robots walking in resonance. *Z. Für Angew. Math. Mech.* **94**, 968–973 (2014). <https://doi.org/10.1002/zamm.201300245>
  66. Faux, D., Thomas, O., Grondel, S., Cattán, É.: Dynamic simulation and optimization of artificial insect-sized flapping wings for a bioinspired kinematics using a two resonant vibration modes combination. *J. Sound Vib.* **460**, 114883 (2019). <https://doi.org/10.1016/j.jsv.2019.114883>
  67. Faux, D., Thomas, O., Cattán, E., Grondel, S.: Two modes resonant combined motion for insect wings kinematics reproduction and lift generation. *EPL Europhys. Lett.* **121**, 66001 (2018). <https://doi.org/10.1209/0295-5075/121/66001>
  68. Miles, J.: Resonance and symmetry breaking for a duffing oscillator. *SIAM J. Appl. Math.* **49**, 968–981 (1989). <https://doi.org/10.1137/0149058>
  69. Liu, Y., Guo, F., He, X., Hui, Q.: Boundary control for an axially moving system with input restriction based on disturbance observers. *IEEE Trans. Syst. Man Cybern. Syst.* **49**, 2242–2253 (2019). <https://doi.org/10.1109/TSMC.2018.2843523>
  70. Liu, Y., Chen, X., Wu, Y., Cai, H., Yokoi, H.: Adaptive neural network control of a flexible spacecraft subject to input nonlinearity and asymmetric output constraint. *IEEE Trans. Neural Netw. Learn. Syst.* (2021). <https://doi.org/10.1109/TNNLS.2021.3072907>
  71. Liu, Y., Mei, Y., Cai, H., He, C., Liu, T., Hu, G.: Asymmetric input–output constraint control of a flexible variable-length rotary crane arm. *IEEE Trans. Cybern.* (2021). <https://doi.org/10.1109/TCYB.2021.3055151>
  72. Liu, Y., Chen, X., Mei, Y., Wu, Y.: Observer-based boundary control for an asymmetric output-constrained flexible robotic manipulator. *Sci. China Inf. Sci.* **65**, 139203 (2022). <https://doi.org/10.1007/s11432-019-2893-y>
  73. Kwak, M.K.: *Dynamic Modeling and Active Vibration Control of Structures*. Springer, Dordrecht (2022)
  74. Min, C., Dahlmann, M., Sattel, T.: A concept for semi-active vibration control with a serial-stiffness-switch system. *J. Sound Vib.* **405**, 234–250 (2017). <https://doi.org/10.1016/j.jsv.2017.06.007>
  75. Min, C., Dahlmann, M., Sattel, T.: Steady state response analysis for a switched stiffness vibration control system based on vibration energy conversion. *Nonlinear Dyn.* **103**, 239–254 (2021). <https://doi.org/10.1007/s11071-020-06147-8>
  76. Jalili, N.: A comparative study and analysis of semi-active vibration-control systems. *J. Vib. Acoust.* **124**, 593–605 (2002). <https://doi.org/10.1115/1.1500336>
  77. Combes, S.A., Gagliardi, S.F., Switzer, C.M., Dillon, M.E.: Kinematic flexibility allows bumblebees to increase energetic efficiency when carrying heavy loads. *Sci. Adv.* **6**, eaay3115 (2020). <https://doi.org/10.1126/sciadv.aay3115>
  78. Lehmann, F.O., Dickinson, M.H.: The changes in power requirements and muscle efficiency during elevated force production in the fruit fly *Drosophila melanogaster*. *J. Exp. Biol.* **200**, 1133 (1997). <https://doi.org/10.1242/jeb.200.7.1133>
  79. Vance, J.T., Altshuler, D.L., Dickson, W.B., Dickinson, M.H., Roberts, S.P.: Hovering flight in the honeybee *Apis mellifera*: kinematic mechanisms for varying aerodynamic forces. *Physiol. Biochem. Zool.* **87**, 870–881 (2014). <https://doi.org/10.1086/678955>
  80. Unwin, D.M., Corbet, S.A.: Wingbeat frequency, temperature and body size in bees and flies. *Physiol. Entomol.* **9**, 115–121 (1984). <https://doi.org/10.1111/j.1365-3032.1984.tb00687.x>
  81. Dickinson, M.: Lighton: muscle efficiency and elastic storage in the flight motor of *Drosophila*. *Science* **268**, 87–90 (1995). <https://doi.org/10.1126/science.7701346>
  82. Whitehead, S.C., Beatus, T., Canale, L., Cohen, I.: Pitch perfect: how fruit flies control their body pitch angle. *J. Exp. Biol.* **218**, 3508–3519 (2015). <https://doi.org/10.1242/jeb.122622>
  83. Ristroph, L., Ristroph, G., Morozova, S., Bergou, A.J., Chang, S., Guckenheimer, J., Wang, Z.J., Cohen, I.: Active and passive stabilization of body pitch in insect flight. *J. R. Soc. Interface* **10**, 20130237 (2013). <https://doi.org/10.1098/rsif.2013.0237>
  84. Muijres, F.T., Elzinga, M.J., Melis, J.M., Dickinson, M.H.: Flies evade looming targets by executing rapid visually directed banked turns. *Science* **344**, 172–177 (2014). <https://doi.org/10.1126/science.1248955>
  85. Greenewalt, C.H.: The wings of insects and birds as mechanical oscillators. *Proc. Am. Philos. Soc.* **104**, 605–611 (1960)
  86. Harne, R.L., Wang, K.W.: Dipteran wing motor-inspired flapping flight versatility and effectiveness enhancement. *J. R. Soc. Interface* **12**, 20141367 (2015). <https://doi.org/10.1098/rsif.2014.1367>
  87. Nachtigall, W., Roth, W.: Correlations between stationary measurable parameters of wing movement and aerodynamic force production in the blowfly (*Calliphora vicina* R.-D.). *J. Comp. Physiol. A* **150**, 251–260 (1983). <https://doi.org/10.1007/BF00606375>

88. Miyan, J.A., Ewing, A.W.: How Diptera move their wings: a re-examination of the wing base articulation and muscle systems concerned with flight. *Philos. Trans. R. Soc. Lond. B Biol. Sci.* **311**, 271–302 (1985). <https://doi.org/10.1098/rstb.1985.0154>
89. Dickinson, M.H., Tu, M.S.: The function of dipteran flight muscle. *Comp. Biochem. Physiol. A Physiol.* **116**, 223–238 (1997). [https://doi.org/10.1016/S0300-9629\(96\)00162-4](https://doi.org/10.1016/S0300-9629(96)00162-4)
90. Somers, J., Georgiades, M., Su, M.P., Bagi, J., Andrés, M., Alampounti, A., Mills, G., Ntabaliba, W., Moore, S.J., Spaccapelo, R., Albert, J.T.: Hitting the right note at the right time: circadian control of audibility in *Anopheles* mosquito mating swarms is mediated by flight tones. *Sci. Adv.* **8**, eabl4844 (2022). <https://doi.org/10.1126/sciadv.abl4844>
91. Verstraten, T., Beckerle, P., Furnémont, R., Mathijssen, G., Vanderborght, B., Lefeber, D.: Series and parallel elastic actuation: impact of natural dynamics on power and energy consumption. *Mech. Mach. Theory* **102**, 232–246 (2016). <https://doi.org/10.1016/j.mechmachtheory.2016.04.004>
92. Wang, S., van Dijk, W., van der Kooij, H.: Spring uses in exoskeleton actuation design. In: *Proceedings of the 2011 IEEE International Conference on Rehabilitation Robotics*, pp. 1–6. IEEE, Zurich (2011)
93. Gau, J., Wold, E.S., Lynch, J., Gravish, N., Sponberg, S.: The hawkmoth wingbeat is not at resonance. *Biol. Lett.* **18**, 20220063 (2022). <https://doi.org/10.1098/rsbl.2022.0063>
94. Zhu, H.J., Sun, M.: Kinematics measurement and power requirements of fruitflies at various flight speeds. *Energies* **13**, 4271 (2020). <https://doi.org/10.3390/en13164271>
95. Dickinson, M.H., Lehmann, F.-O., Sane, S.P.: Wing rotation and the aerodynamic basis of insect flight. *Science* **284**, 1954 (1999). <https://doi.org/10.1126/science.284.5422.1954>
96. Robertson, B.D., Sawicki, G.S.: Unconstrained muscle-tendon workloops indicate resonance tuning as a mechanism for elastic limb behavior during terrestrial locomotion. *Proc. Natl. Acad. Sci.* **112**, E5891–E5898 (2015). <https://doi.org/10.1073/pnas.1500702112>
97. Josephson, R.K., Malamud, J.G., Stokes, D.R.: Power output by an asynchronous flight muscle from a beetle. *J. Exp. Biol.* **203**, 2667 (2000). <https://doi.org/10.1242/jeb.203.17.2667>
98. Sun, M., Tang, J.: Unsteady aerodynamic force generation by a model fruit fly wing in flapping motion. *J. Exp. Biol.* **205**, 55–70 (2002). <https://doi.org/10.1242/jeb.205.1.55>
99. Stramigioli, S., van Oort, G., Dertien, E.: A concept for a new energy efficient actuator. In: *Proceedings of the 2008 IEEE/ASME International Conference on Advanced Intelligent Mechatronics*, pp. 671–675. IEEE, Xian (2008)
100. Berret, B., Darlot, C., Jean, F., Pozzo, T., Papaxanthis, C., Gauthier, J.P.: The inactivation principle: mathematical solutions minimizing the absolute work and biological implications for the planning of arm movements. *PLOS Comput. Biol.* **4**, e1000194 (2008). <https://doi.org/10.1371/journal.pcbi.1000194>
101. Graham, R.L., Knuth, D.E., Patashnik, O.: *Concrete Mathematics: A Foundation for Computer Science*. Addison-Wesley, Reading (1994)
102. Verstraten, T., Mathijssen, G., Furnémont, R., Vanderborght, B., Lefeber, D.: Modeling and design of geared DC motors for energy efficiency: comparison between theory and experiments. *Mechatronics* **30**, 198–213 (2015). <https://doi.org/10.1016/j.mechatronics.2015.07.004>
103. Kelly, M.: An introduction to trajectory optimization: how to do your own direct collocation. *SIAM Rev.* **59**, 849–904 (2017). <https://doi.org/10.1137/16M1062569>
104. Vanderborght, B., Van Ham, R., Lefeber, D., Sugar, T.G., Hollander, K.W.: Comparison of mechanical design and energy consumption of adaptable, passive-compliant actuators. *Int. J. Robot. Res.* **28**, 90–103 (2009). <https://doi.org/10.1177/0278364908095333>
105. Moon, J.-S., Bae, J.: Gait optimization and energetics of ballistic walking for an underactuated biped with knees. *Nonlinear Dyn.* **85**, 1533–1546 (2016). <https://doi.org/10.1007/s11071-016-2777-2>
106. Haberland, M., Kim, S.: On extracting design principles from biology: II. Case study—the effect of knee direction on bipedal robot running efficiency. *Bioinspir. Biomim.* **10**, 016011 (2015). <https://doi.org/10.1088/1748-3190/10/1/016011>
107. Berret, B., Chiovetto, E., Nori, F., Pozzo, T.: Evidence for composite cost functions in arm movement planning: an inverse optimal control approach. *PLOS Comput. Biol.* **7**, e1002183 (2011). <https://doi.org/10.1371/journal.pcbi.1002183>
108. Oguz, O.S., Zhou, Z., Wollherr, D.: A hybrid framework for understanding and predicting human reaching motions. *Front. Robot. AI* **5**, 27 (2018). <https://doi.org/10.3389/frobt.2018.00027>
109. Reid, H.E., Schwab, R.K., Maxcer, M., Peterson, R.K.D., Johnson, E.L., Jankauski, M.: Wing flexibility reduces the energetic requirements of insect flight. *Bioinspir. Biomim.* **14**, 056007 (2019). <https://doi.org/10.1088/1748-3190/ab2dbc>
110. Margaria, R.: *Biomechanics and Energetics of Muscular Exercise*. Clarendon, Oxford (1979)
111. Ruina, A., Bertram, J.E.A., Srinivasan, M.: A collisional model of the energetic cost of support work qualitatively explains leg sequencing in walking and galloping, pseudo-elastic leg behavior in running and the walk-to-run transition. *J. Theor. Biol.* **237**, 170–192 (2005). <https://doi.org/10.1016/j.jtbi.2005.04.004>
112. Alexander, R.M.: A model of bipedal locomotion on compliant legs. *Philos. Trans. R. Soc. Lond. B. Biol. Sci.* **338**, 189–198 (1992). <https://doi.org/10.1098/rstb.1992.0138>
113. Jordan, H.E.: *Energy-Efficient Electric Motors and their Applications*. Springer, Dordrecht (1994)
114. Okay, A., Khamesee, M.B., Erkorkmaz, K.: Design and optimization of a voice coil actuator for precision motion applications. *IEEE Trans. Magn.* **51**, 1–10 (2015). <https://doi.org/10.1109/TMAG.2014.2381160>
115. Kumar, M., Walkama, D.M., Guasto, J.S., Ardekani, A.M.: Flow-induced buckling dynamics of sperm flagella. *Phys. Rev. E* **100**, 063107 (2019). <https://doi.org/10.1103/PhysRevE.100.063107>
116. Beatus, T., Guckenheimer, J., Cohen, I.: Controlling roll perturbations in fruit flies. *J. R. Soc. Interface* (2015). <https://doi.org/10.1098/rsif.2015.0075>

117. Kato, N., Ayers, J., Morikawa, H. (eds.): Bio-mechanisms of Swimming and Flying. Springer, New York (2004)
118. Cator, L.J., Arthur, B.J., Harrington, L.C., Hoy, R.R.: Harmonic convergence in the love songs of the dengue vector mosquito. *Science* **323**, 1077–1079 (2009). <https://doi.org/10.1126/science.1166541>
119. Spangler, H.G., Buchmann, S.L.: Effects of temperature on wingbeat frequency in the solitary bee *Centris caespaliniae* (Anthophoridae: Hymenoptera). *J. Kans. Entomol. Soc.* **64**, 107–109 (1991)
120. Ben-Dov, O., Beatus, T.: Pose estimation of free-flying fruit flies. In: Presented at the 25th International Conference on Pattern Recognition, Milan, Italy (2021)
121. De Silva, C.W.: Vibration and Shock Handbook. CRC Press, Boca Raton (2005)
122. Cai, L.-W.: Fundamentals of Mechanical Vibrations. ASME/Wiley, Hoboken (2016)
123. Sun, M.: Insect flight dynamics: stability and control. *Rev. Mod. Phys.* **86**, 615–646 (2014). <https://doi.org/10.1103/RevModPhys.86.615>
124. Ma, K.Y., Chirarattananon, P., Fuller, S.B., Wood, R.J.: Controlled flight of a biologically inspired, insect-scale robot. *Science* **340**, 603–607 (2013). <https://doi.org/10.1126/science.1231806>
125. Huang, S., Wensman, J.P., Ferris, D.P.: Locomotor adaptation by transtibial amputees walking with an experimental powered prosthesis under continuous myoelectric control. *IEEE Trans. Neural Syst. Rehabil. Eng.* **24**, 573–581 (2016). <https://doi.org/10.1109/TNSRE.2015.2441061>
126. Edwards, C., Spurgeon, S.K.: Sliding Mode Control. CRC Press, Boca Raton (1998)
127. Kwatny, H.G., Blankenship, G.: Nonlinear Control and Analytical Mechanics. Birkhauser, Boston (2000)
128. Popovic, M.B.: Biomechatronics. Academic Press, Cambridge (2019)

**Publisher's Note** Springer Nature remains neutral with regard to jurisdictional claims in published maps and institutional affiliations.

Springer Nature or its licensor holds exclusive rights to this article under a publishing agreement with the author(s) or other rightsholder(s); author self-archiving of the accepted manuscript version of this article is solely governed by the terms of such publishing agreement and applicable law.